JGR Space Physics

RESEARCH ARTICLE
10.1029/2020JA028916

Key Points:

- Localized stalling of the thermospheric cross-polar jet was observed equatorward of the auroral zone
- Stalling occurs over short meridional distances of ~100–200 km
- Abrupt stalling was found to occur more frequently during quiet solar and geomagnetic conditions

Correspondence to:
R. Itani,
ritani@alaska.edu

Citation:
Itani, R., & Conde, M. (2021). Characterizing unexpectedly localized slowing of the thermospheric cross-polar jet of neutral wind over Alaska in the midnight sector. *Journal of Geophysical Research: Space Physics*, *126*, e2020JA028916. https://doi.org/10.1029/2020JA028916

Received 20 NOV 2020
Accepted 21 AUG 2021

Characterizing Unexpectedly Localized Slowing of the Thermospheric Cross-Polar Jet of Neutral Wind Over Alaska in the Midnight Sector

R. Itani[1] **and M. Conde**[1]

[1]Geophysical Institute, University of Alaska Fairbanks, Fairbanks, AK, USA

Abstract We have measured auroral zone thermospheric neutral winds in the midnight local time sector, using ground-based optical Doppler spectroscopy of the 630.0 nm emission from atomic oxygen, originating at around 240 km altitude over Alaska. One of the most prominent features seen in winds at these latitudes is the cross-polar jet emerging from the polar cap at local times around magnetic midnight. The standard view is that wind flows anti-sunward in the midnight sector and spills equatorward over magnetic latitudes extending well below those of the auroral zone. The purpose of this paper is to show that this view is too simplistic. From our observatory at Poker Flat, Alaska (~65.12^{o}N), the anti-sunward flow is frequently seen to stall over surprisingly short horizontal distances (100–200 km), without spilling further equatorward. This behavior is most prevalent during a low solar activity at mid-winter when the combination of pressure gradient established by solar heating and the ion drag is not enough to allow the jet to push through the background atmosphere on the nightside. At higher latitudes, by contrast, the flow is relatively uniformly anti-sunward around magnetic midnight even during quiet conditions. During periods of high solar and magnetic activity, the expected spilling of the midnight sector cross-polar jet to lower latitudes often is indeed observed over Alaska. Our observation of abrupt stalling during quiet solar and geomagnetic conditions is a very significant difference from the model predictions, with potentially important ramifications- which is the motivation for the present study.

Plain Language Summary We have analyzed ground-based remote sensing measurements of thermospheric neutral winds above Alaska, at 240 km altitude. In particular, we have studied how space weather affects the well-known large-scale flow that carries winds from the sunlit dayside of the Earth across the polar cap into the night side. This powerful flow feature is typically expected to emerge from the polar cap in the midnight sector and continue blowing equatorward well into sub-auroral latitudes. However, our data show instances in which the equatorward flow instead stalls over Alaska in an unexpectedly abrupt manner. We have explored the conditions under which this abrupt stalling occurs, and commented on the consequences that this behavior might have on technological systems that depend on accurate models of thermospheric wind fields.

1. Introduction

Earth's thermosphere is the region of atmosphere from ~90 km up to ~500–1,000 km altitude depending on solar-cycle conditions. Its lower edge is defined by the transition to a positive vertical temperature gradient above the mesopause, whereas the upper limit is generally taken to be the height at which the mean free path exceeds one scale height. The upper portion of the thermosphere corresponds to the altitude region occupied by low Earth-orbiting spacecraft. Understanding the details of the weather in the thermosphere is thus important for orbital prediction and for space debris collision avoidance. The dominant terms involved in orbital predictions are obtained from the direct application of well-known equations of Newtonian mechanics. However, operational responses to space debris hazards are driven by the uncertainty in these predictions, on the time scales of days to a week or so ahead. The largest contribution to this uncertainty comes from aerodynamic drag effects, due to imperfect knowledge of the (vector) wind and (scalar) mass density fields of the ambient atmosphere. Thus, in order to reduce these uncertainties, an accurate thermospheric model, including wind, is needed.

Motivated by the need to improve our detailed understanding of thermospheric dynamics, we have measured winds at *F*-region heights in the auroral zone, using passive ground-based optical Doppler spectroscopy. In this work we have focused on a flow feature within the thermosphere that we refer to as the "cross-polar jet" (e.g., Conde et al., 2001; Smith et al., 1998). This is a strong large-scale coherent wind flow that, at altitudes above ~150 km, transports air parcels antisunward from the dayside of the polar cap to the nightside. The cross-polar jet is embedded in the large-scale thermospheric meteorological system that in mid and low latitudes is driven by the solar pressure gradient being balanced by a combination of ion drag, viscosity, and Coriolis effect (Killeen & Roble, 1984). At latitudes poleward of $\pm 65^{o}$, ion drag often dominates energy and momentum input during elevated geomagnetic activity (Kelley et al., 1977; Killeen et al., 1982; Meriwether et al., 1973; Roble et al., 1983). The large-scale thermospheric meteorology of the whole planet is well represented by the superposed actions of these forces (Liuzzo et al., 2015).

While ion drag and the solar pressure gradient tend to oppose each other at auroral latitudes in the evening and morning sectors, they act together throughout the polar cap, with both driving antisunward flow. This co-aligned forcing acting over a large geographic area is the origin of the cross-polar jet (Meriwether et al., 1988). Modeling typically suggests that the cross-polar jet would spill out of the polar cap on the nightside and continue flowing for many degrees of latitude equatorward of the auroral zone. Examples of this "spilling out" have been presented, for example, by Heelis et al. (1982) and in Figure 3 from Dhadly et al. (2018).

Even though the cross-polar jet is a well-formed and powerful flow feature, we have observed that, under certain conditions, it appears to stall surprisingly suddenly upon exiting the polar cap. That is, the stalling can occur very abruptly over a streamwise distance of only a few hundred kilometers or less. We have observed instances where the cross-polar jet is stopped, deflected, or even reversed in the midnight sector, so that it may even blow sunward. We refer to this class of phenomena using the umbrella term of "stalling" of the cross-polar jet. This puzzling behavior has been observed previously, for example, shown in Figure 11 of Conde et al. (2018). This figure presents the neutral horizontal wind field at *F*-region heights derived by merging SDI data from Toolik Lake, Poker Flat, and Gakona Alaska, using localized basis function fitting. The figure shows winds near midnight magnetic local time (MLT) [11 UT], and stalling is apparent over southern Alaska, at a slightly lower latitude than we report in this study. However, while the stalling was noted in this prior work, it was not examined in detail.

Because the thermosphere is convectively stable and has very high kinematic viscosity (Yerg, 1952), structures in the wind on small spatial scales (200 km or less) are not predicted to be significant (Killeen & Roble, 1988; Killeen et al., 1988; Smith et al., 1988). The net effect of convective stability and high kinematic viscosity is to suppress small-scale vortices and convective overturning, thereby producing a wind field that is expected to be smooth, laminar, and not strongly dependent on altitude above 200 km. Stalling of the cross-polar jet that we have actually observed occurs much more abruptly than expected based on these considerations, suggesting that there must be a specific process that is actively causing the cross-polar jet to stall.

The complete set of *F*-region wind forcing terms includes drivers from the *E*-region and below, that could potentially impose additional variability onto the cross-polar jet (beyond that due solely to solar and magnetic activity). However, in the present work, we have not explicitly studied these potential driving forces from below, because the combination of seasonal, solar, and geomagnetic activity already appear to mostly explain the responses that we observe. Future work may address forcing from below, but this is beyond the scope of the current study.

2. Instruments and Methods

Various techniques have been used since the 1960s to measure thermospheric winds. One of the most productive has been to measure Doppler shifts of naturally occurring atmospheric optical emissions, such as the 630.0 nm spectra, using Fabry-Perot interferometers (FPIs). Here, we have analyzed the spectra of the 630.0 nm atomic oxygen emission from aurora/airglow to derive estimates of winds at ~240 km altitude. In the thermosphere, atomic oxygen is mainly created by photodissociation of molecular oxygen and ozone (Banks & Kockarts, 1973; McGrath & McGarvey, 1967). Red line optical emission (630.0 nm) is produced

both by airglow and aurora and corresponds to the 1D to 3P transition of excited oxygen atoms. The radiative lifetime of the excited 1D state of atomic oxygen is estimated to be ~114 s (Slanger & Copeland, 2003). Thus significant red line emission is possible only at higher altitude (~200 km or higher) where the atmospheric density is very low and the frequency of collisional quenching is also low relative to the radiative lifetime. Although the 630.0 nm emission spans a wide and somewhat variable range of altitudes, the vertical gradient of the wind field is typically weak at heights above 220 km (Hedin et al., 1988). Hence, this well-known "red line" emission is thought to be a reasonably reliable indicator of the *F*-region of thermosphere (McCormac et al., 1987).

Data presented here are based on spectra obtained by an all-sky imaging FPI. The particular type of instrument used is known as a Scanning Doppler Imager (SDI). Although we have data available from six such SDIs, most results presented here were obtained from the instrument at Poker Flat, Alaska (~65.12 N). The instruments and observing techniques are described by Conde and Smith (1995, 1997, 1998), Anderson et al. (2012a), and Conde et al. (2018). SDIs resolve the visible sky into a software-defined set of sub-regions and compile a high-resolution Doppler spectrum of the airglow/auroral emission for each sub-region. The current version of the instrument typically resolves the field of view into 115 sub-regions termed "zones" as per the techniques described by Conde and Smith (1997). These spectra are then used to infer Doppler line-of-sight (LOS) wind measurements and Doppler temperatures, as described by Conde et al. (2001). Several methods currently are employed for utilizing these LOS observations to infer three-component wind fields at the height of the atmospheric optical emission layer. Here we present the results based on the simple "monostatic" wind fitting algorithm described by Conde and Smith (1998). For comparison to the SDI observations, we have presented winds predicted by the Thermosphere Ionosphere Electrodynamics General Circulation Model (TIEGCM) (Richmond et al., 1992) and by the HWM14 empirical model.

3. Results

This particular study examines the behavior of *F*-region winds around midnight MLT and, in particular, instances where the cross-polar jet was observed to stall over Alaska. It is focused on Poker Flat, Alaska, mainly because most other SDI instruments are located further poleward and hence less favorably positioned to observe the emergence of the cross-polar jet from the polar cap. For this study, we examined SDI data going back to the last solar maximum (2014), which indicated that as solar activity declined at the end of solar cycle 24, the instances of stalling of the cross-polar jet have increased. We did operate an SDI FPI at a lower latitude site, at Gakona, Alaska (~62.39°N) between 2009 and 2014. As discussed below, this instrument did observe instances of stalling, but only during periods outside of solar maximum.

A salient feature of the stalling phenomenon is that it happens suddenly, over a short horizontal distance. While it could potentially be characterized by averaging the wind fields over multiple days when stalling occurred, the location of the stalling would likely vary between these days, resulting in an average wind field that would blur the sharp transition that actually occurs on the individual contributing days. Thus, we instead demonstrate the phenomenon by presenting data from a number of example days when the cross-polar jet emerges as expected and, by contrast, from days when the jet is stalled. In surveying the available data to compile statistics and choose example days, we rejected periods of cloudy sky conditions and when instrumental issues produced implausible wind fields. As a result of the survey, we focus here on six selected days when we observed simple examples of stalling, and a contrasting six days when the jet emerged from the polar cap without stalling. The ultimate goal is to infer the mechanism(s) responsible for the sudden stalling by characterizing its morphology and the conditions under which it occurs. For this purpose, we characterized the background geophysical conditions according to the season, $F_{10.7}$ and K_p indices, local magnetic & auroral activity, and using the Akasofu's "epsilon" parameter (Perreault & Akasofu, 1978) that is often used as a proxy for the rate of solar wind energy transfer into the magnetosphere.

3.1. Wind Dial Plots

Figures 1–5 present winds observed from Poker Flat using a "dial" plot format. Figure 1 should be imagined as a view looking down on Earth from above the north polar region, with the magnetic north pole at the center of the dial plot. The sunward direction is toward the top of the page, and the observatory location

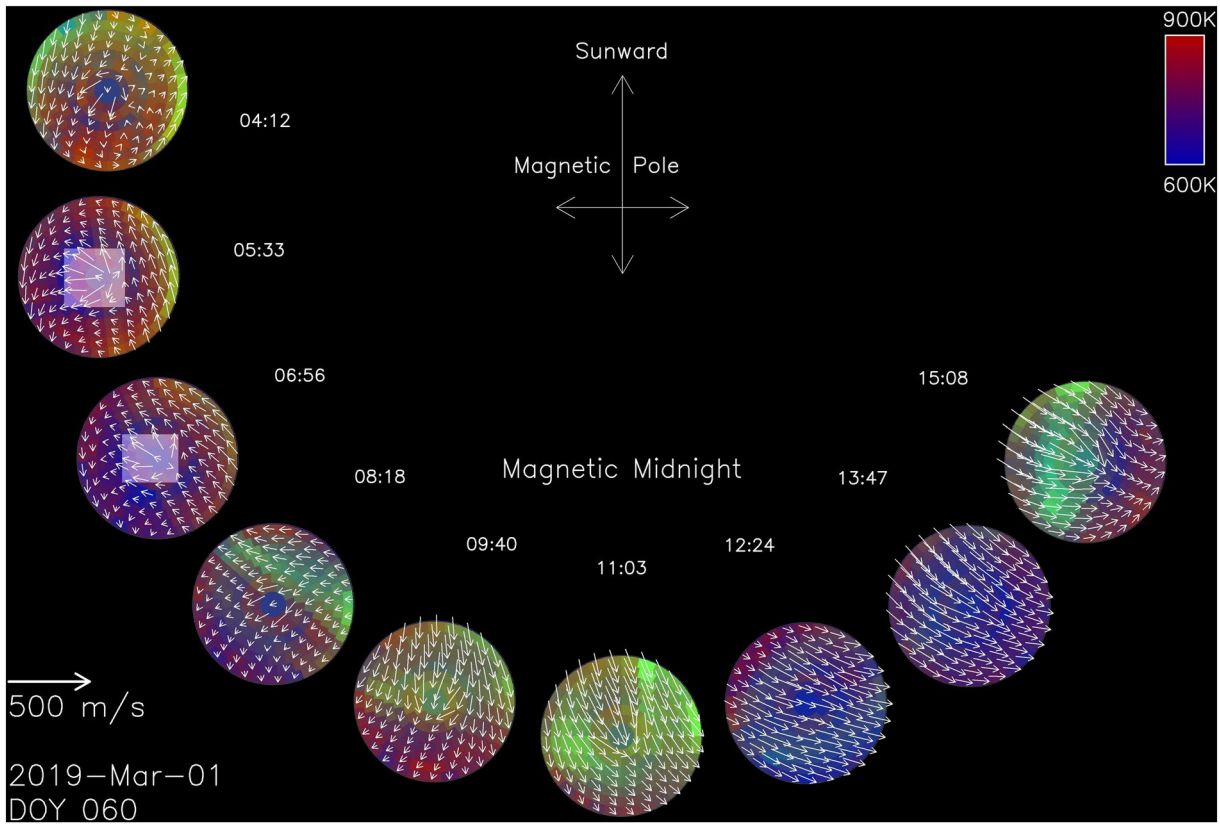

Figure 1. Example wind dial plot for the day of March 01, 2019. Here, each circle represents the nearly all-sky field of view at the indicated UT time. The center of the circle corresponds to viewing in the zenith, whereas the outer edge represents the lowest elevation included in the field of view. Magnetic local times vary around the dial: the top of the dial corresponds to local magnetic noon, whereas towards the bottom is magnetic midnight. The sunward direction is, therefore, toward the top of the page everywhere across the plot. Green hues depict the airglow/auroral emission brightness at 630.0 nm in arbitrary units, whereas blue through red colors represent temperature derived from Doppler spectral widths, as indicated by the color scale bar at the top right of the figure. Note that hues representing temperature are more stable from one plotted time to the next than is the case for the emission brightness. This is because fractional variations are smaller and smoother in temperature than in brightness, both spatially and temporally. White arrows show the wind speed and direction, with speeds being proportional to the arrow length, as indicated by the scale arrow. The format of this plot does not permit winds to be shown with the full time resolution of the measurements, so we have plotted only a temporally sub-sampled set of measurements to describe the whole night. Minor wind artifacts in zones near the zenith are highlighted by rectangles for times of 5:33 UT and 6:56 UT. Similar artifacts appear on occasions in other plots.

advances anticlockwise around the plot with time as Earth rotates. Figures 2–5 are compilations of portions of a wind dial plot presented in same format as Figure 1, but zoomed-in, to show only the midnight sector. In Figures 2, and 3, we have plotted a set of nights when there is no stalling, whereas Figures 4, and 5 present examples of the cross-polar jet stalling within the latitude band observed from our observatory. These plots show wind fields derived from the atomic oxygen red line (630.0 nm) optical emission.

Numerous studies demonstrate that the red line emission typically peaks at ~240 km altitude (Bates, 1978; Witasse et al., 1999; de Meneses et al., 2008). Thus winds and temperatures measured from this emission originate from a circular field of view that spans around 1,100 km in diameter (Conde et al., 2018). Based on this, Figures 6 and 7 use a simple tangent function to map observation zenith angles to radial distance from the observatory, and a two-dimensional interpolation scheme to construct time histories of the winds as a function of magnetic latitude. Background colors in these figures denote the magnetic meridional component of the wind field, whereas black arrows denote the full two-component horizontal wind vectors. The vector components are aligned to magnetic coordinate directions which, at Poker Flat, are rotated ~22° eastward from geographic coordinates.

From these data, we can predict the length scale over which the stalling occurs. However, estimation of this distance is not straightforward to do from data shown in the sky map format of the dial plots (Figures 4 and 5). This is because radial distances between rings of zones in the dial plot sky maps correspond to

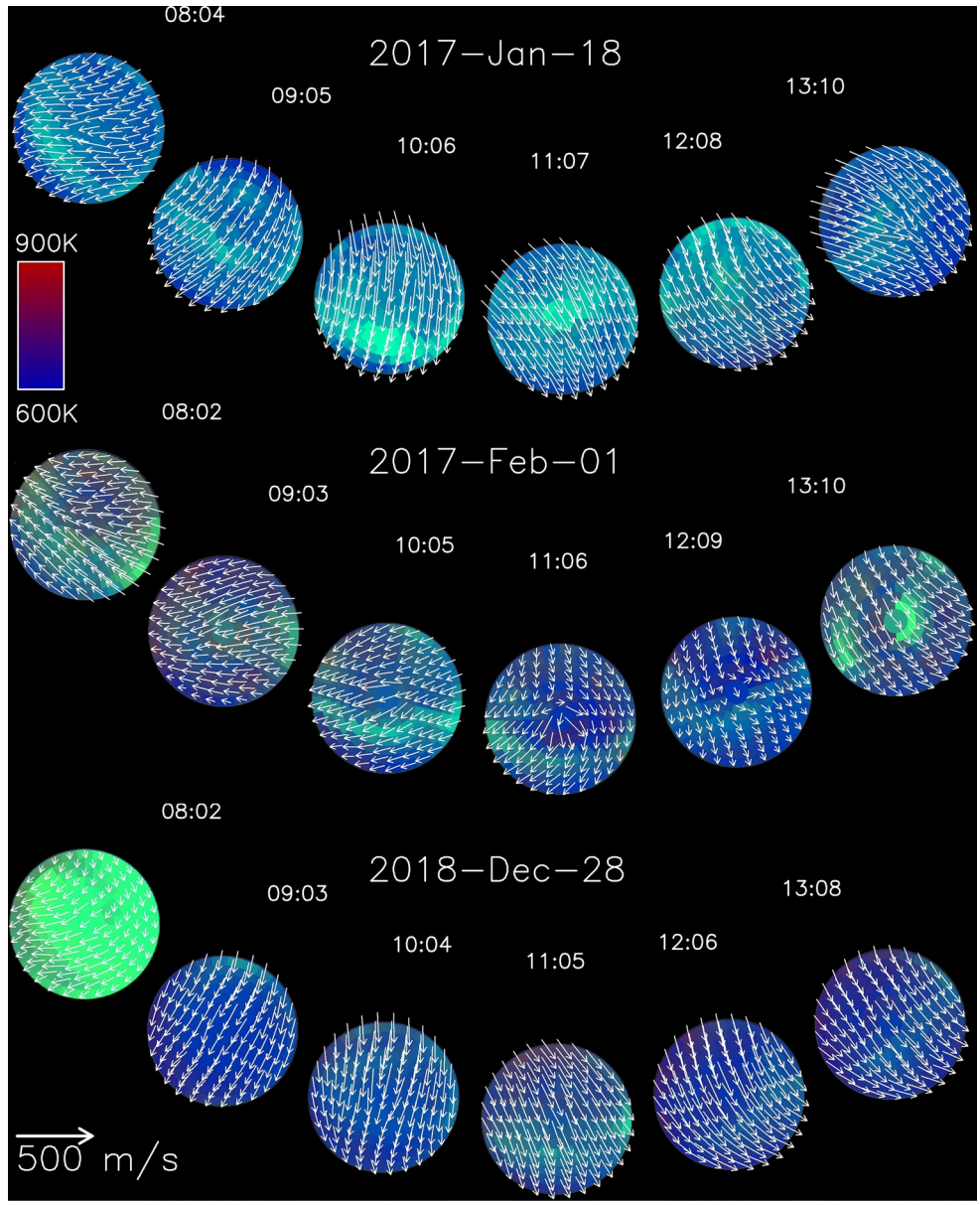

Figure 2. This figure shows just the midnight sector of the dial plots (e.g., Figure 1) compiled together showing three nights (January 18, 2017, February 01, 2017, and December 28, 2018) from Poker Flat, Alaska on which the cross-polar wind jet emerged from the polar cap without stalling (time is shown in UT.) Green hues depict the airglow/auroral intensity, whereas blue through red colors represent temperature derived from Doppler spectral widths as indicated by the color scale bar near the top left of the figure. White arrows show the wind speed and direction, with speeds being proportional to the arrow length as indicated by the scale arrow at the bottom left of the plot.

approximately uniform increments of zenith angle. Instead, it is simpler to examine data in the format of Figure 7 in which neutral meridional winds are mapped over geomagnetic latitude. As we can see between 10:00 UT and 12:30 UT the cross-polar jet stalled within a distance of roughly two degrees of latitude, or ~200 km. This estimate is consistent with the stagnation distance seen in Figure 11 of Conde et al. (2018). That figure shows neutral wind vectors (orange arrows) overlaid onto a geographic map of Alaska. Bistatic trigonometric analysis of similar data to that of the present study was used by Conde et al. (2018) to derive the vectors shown in their Figure 11. The orange arrows in that figure are shown at the maximum spatial resolution possible with these instruments. We estimate from their Figure 11 that the stalling of the wind occurred over a horizontal distance of ~150 km. We cite this example first because it is already published

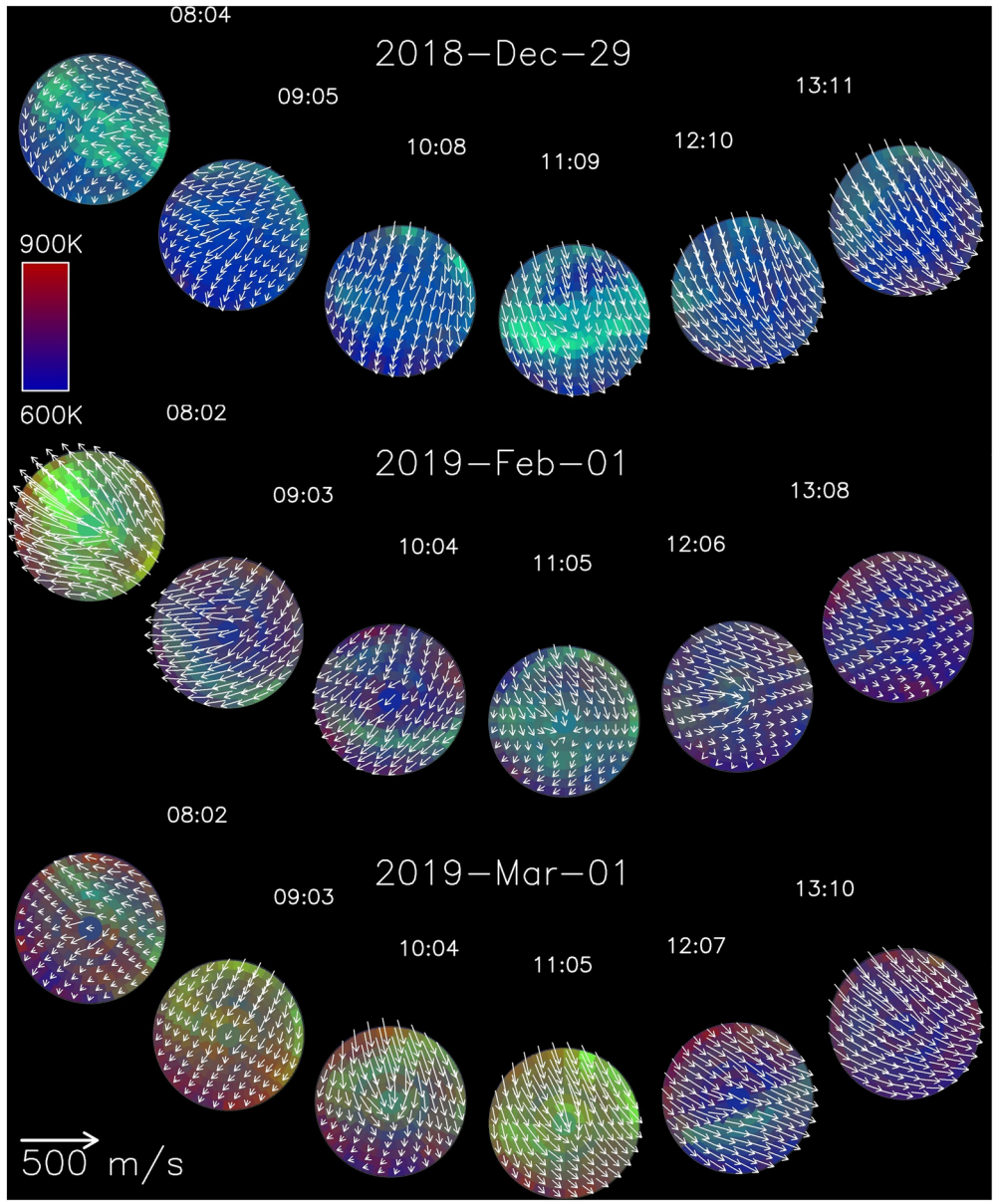

Figure 3. This figure is of the same format as Figure 2 but showing the emergence of the cross-polar jet from the polar cap during the nights of December 29, 2018, February 01, 2019, and March 01, 2019, as seen from Poker Flat, Alaska.

and, second, because stalling occurred over one of the shortest distances that we have seen, based on many years of observations. More typically, stalling is a little less abrupt, leading to our estimate of 200 km stalling distance as being typical of more common cases.

3.2. Artifacts and Uncertainties

Note that some wind maps show artifacts near the center of the field of view (e.g., Figure 1). There are two main reasons for these artifacts. First, the line-of-sight component of the horizontal wind is small when viewing near the zenith, which tends to amplify the effects of any measurement errors on horizontal winds inferred in these regions. Second, there are subtle effects associated with the way the instrument compiles Fabry-Perot fringe images into spectra that make zones near the center more likely to experience the artifacts. These artifacts only apply to the observations near the zenith, and should not impact our ability to characterize stalling, which is seen not only in the zenith but also extending across

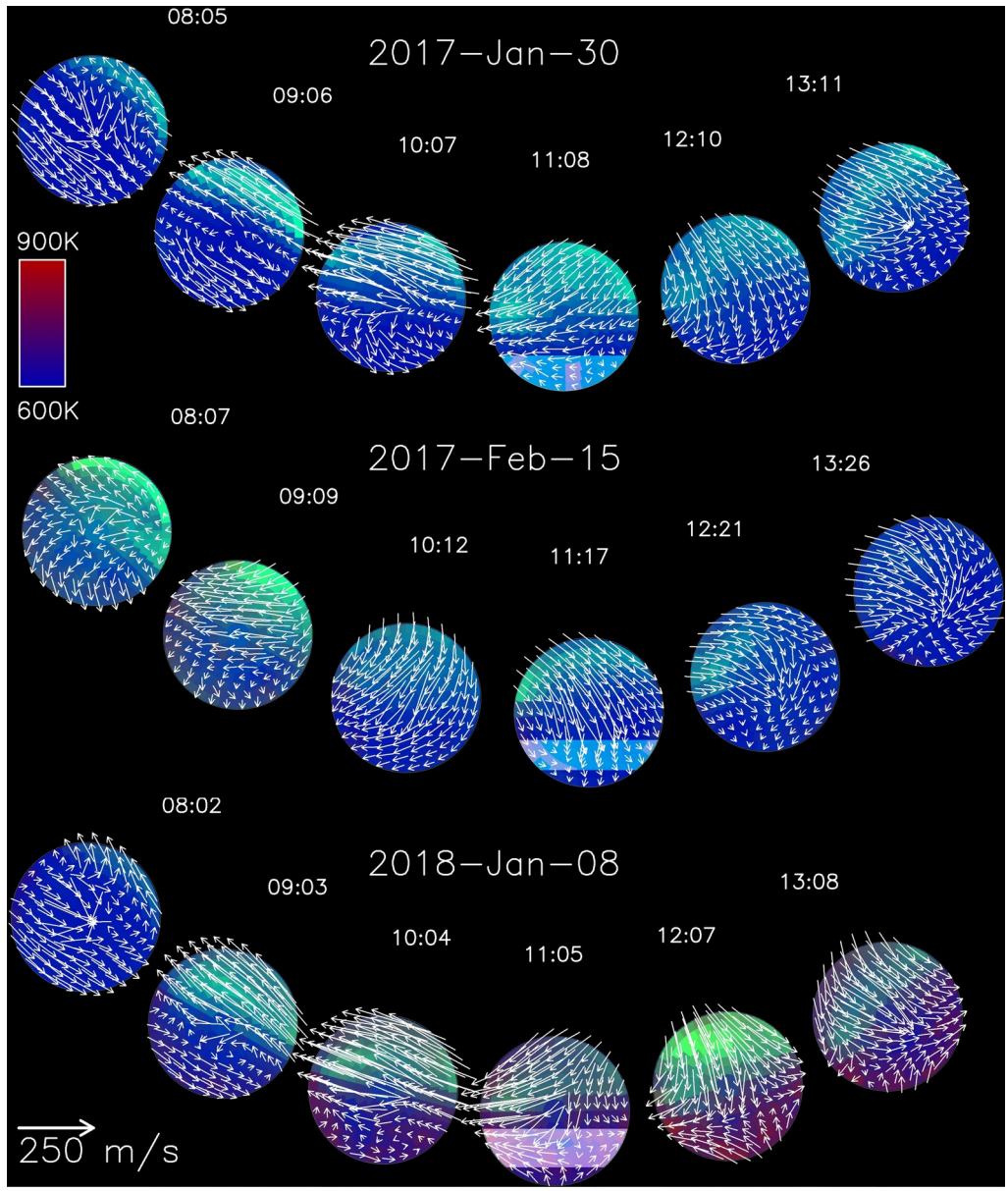

Figure 4. Three nights of data (January 30, 2017, February 15, 2017, and January 08, 2018) during which the cross-polar jet stalled over Poker Flat, Alaska. The format of this plot is the same as in Figures 2 and 3, although we have used a different wind scale because winds on the stalled nights tend to be weaker. The change in scale makes the length of wind vectors in this plot twice as long for a given wind speed as is the case in Figure 2. Regions of stalling of the cross-polar jet have been highlighted only near the local magnetic midnight at times 11:08 UT, 11:17 UT, and 11:05 UT on the first, second, and third rows respectively. We have done this because it is more difficult to interpret slowing of the equatorward flow as stalling at local times away from magnetic midnight. However, there are instances in which stalling does indeed occur beyond the midnight sector, for example, as seen at 12:07 UT on January 08, 2018.

a wide swath of the field of view. In particular, the way the SDI operates makes it insensitive to the spatial gradients in the auroral brightness across its field of view. This is because for the SDI, the spectral information is not encoded as a function of radial position on the detector, rather spectral information is encoded as a function of the scan of the etalon over time. As such, spatial gradients have essentially no effect on the accumulated spectra. However, changes in brightness over time potentially can have an effect, although the SDI suppresses this in two ways. First, spectral data taken over multiple etalon scans are co-added such that effects of temporal changes are most likely to be uncorrelated between scans and

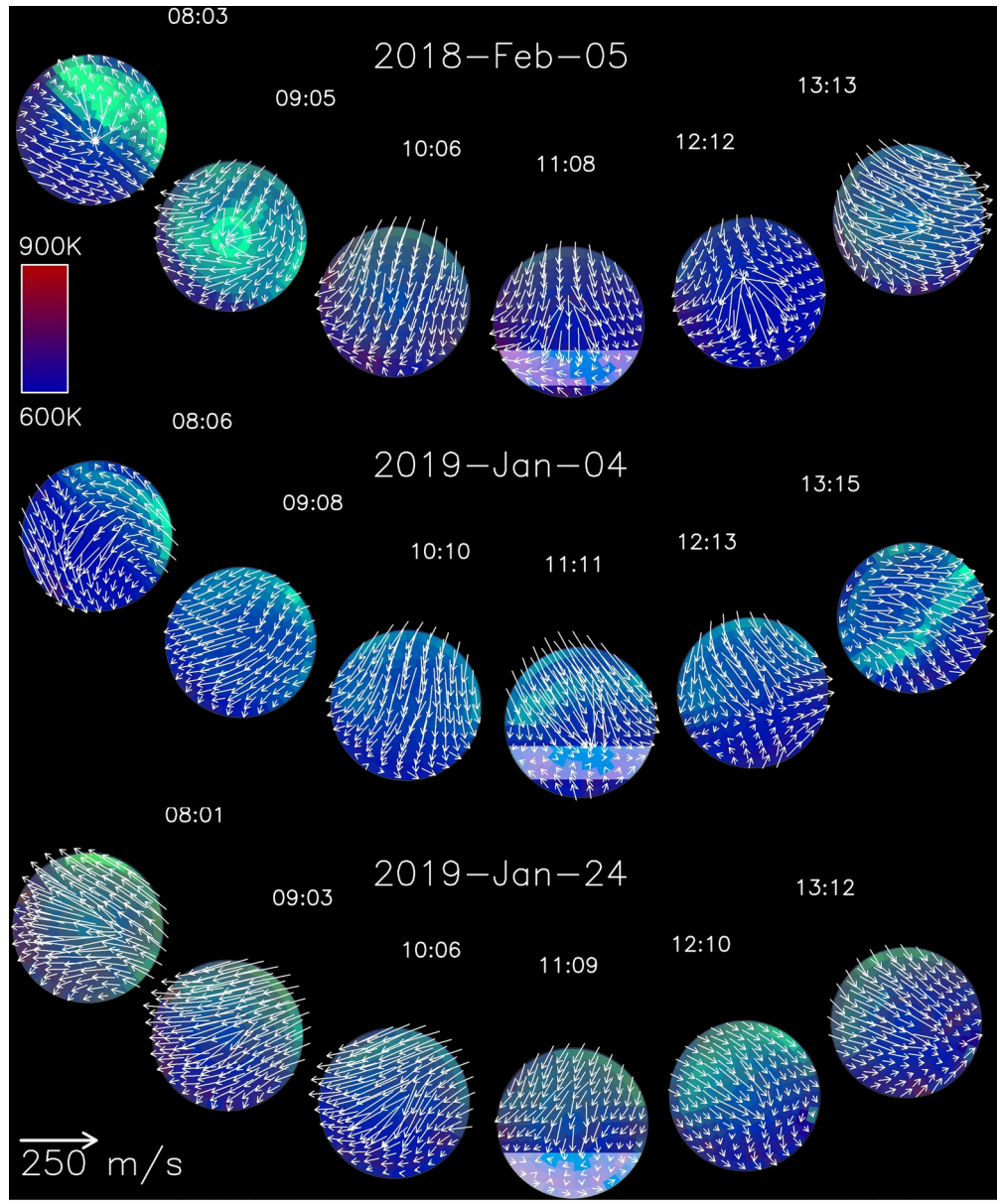

Figure 5. Here we have the same format as Figure 4 except for the nights of February 05, 2018, January 04, 2019, and January 24, 2019. As before, regions of stalling have been highlighted at times 11:08 UT, 11:11 UT, and 11:09 UT respectively.

therefore average to zero. Second, away from the zenith, each zone sums many different spectral phases at any given time. This also has the effect of averaging out temporal variations because any such artifacts are distributed in an uncorrelated fashion across essentially the entire free spectral range spanned by the spectra.

Figure 8 shows an example of the range of uncertainties in the line-of-sight (LOS) component of the wind observed on one particular night. We do not have a direct estimate of the uncertainty in the individual vector wind components. This is because there is a potentially significant contribution to that uncertainty associated with the degree to which the substantial assumptions required by the monostatic fitting algorithm actually held in the real atmosphere at any given time. We do however have empirical experience of the likely uncertainties, based on comparison of monostatic wind fitting (as is used here) versus multistatic fitting, in which the previous assumptions are not required (Anderson

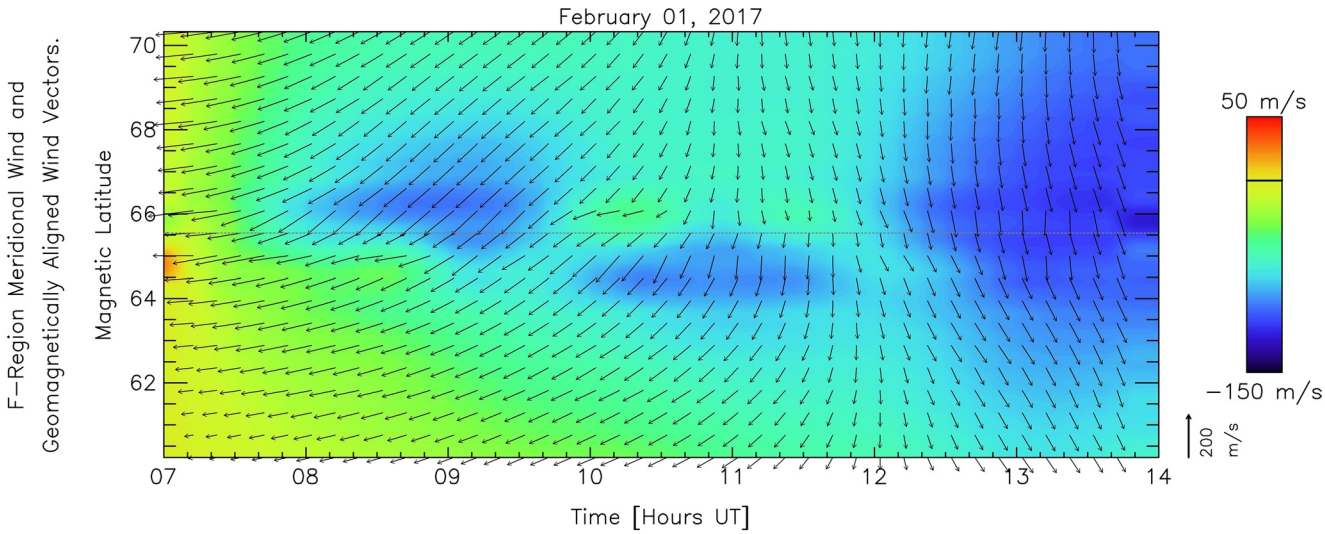

Figure 6. Latitudinal profile of F-region meridional wind, depicted by the background color hue, as a function of local time for the day of February 01, 2017. This plot shows the emergence of the cross-polar jet over the latitude of Poker Flat, Alaska (dashed horizontal line). The color bar at the right indicates the magnitude of meridional wind speed. Arrows in the plot show geomagnetically aligned wind vectors as indicated by the wind scale at the bottom right of the plot.

et al., 2012a, 2012b, 2012c). These comparisons show that, in most cases, errors associated with breakdown of the monostatic assumptions are unlikely to exceed those of the simple statistical uncertainties in the original measurements shown for example in Figure 8. The median LOS wind uncertainty on this night was 10.3 m/s. Based on this prior experience, we expect that uncertainty in the vector wind components would not exceed twice the median value for the LOS uncertainties. On this particular night the optical signal was weak early on. Data from this period contribute most to the histogram peak to the right in Figure 8, at larger uncertainties. Auroral activity increased later in the night, resulting in a second peak in Figure 8 at lower uncertainty values due to the stronger signal. It is seen

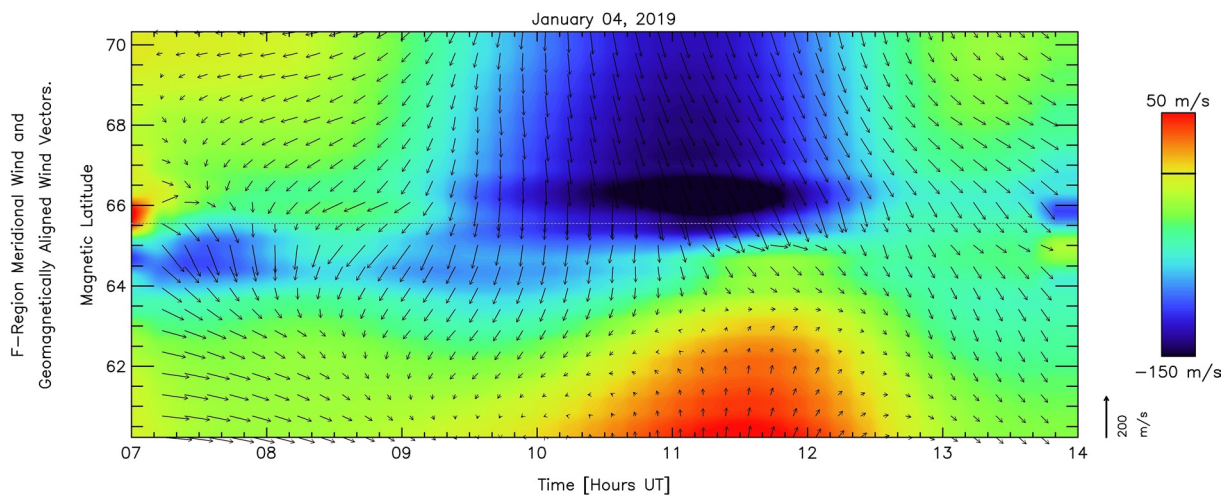

Figure 7. Same format as Figure 6 but for the day of January 04, 2019 and now showing the stalling of the cross-polar wind jet. The large region of blue colored hue represents the cross-polar jet, which is seen to stall just equatorward of Poker Flat between roughly 10–13 h UT. Here, same wind scale is used as in Figure 6.

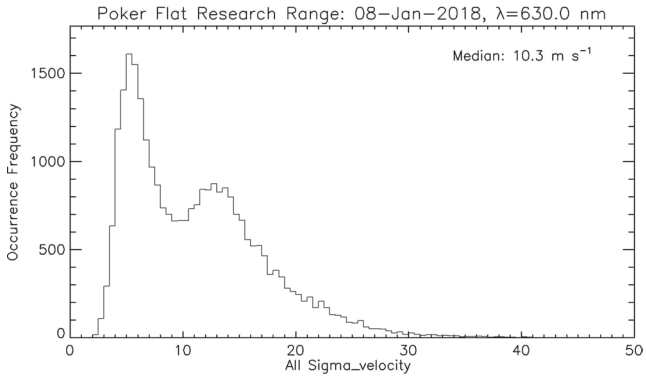

Figure 8. Histogram showing uncertainties in estimates of the line-of-sight (LOS) component of the wind as observed from Poker Flat Research Range on the night of January 8, 2018. The horizontal axis represents the uncertainties that arose from fitting model spectra to the observed spectra, which is a required step in estimating the LOS wind components.

from Figure 8 that even with the weak signal the uncertainty is just ~14 m/s typically and when there is stronger signal the uncertainty drops down to about ~5 m/s.

3.3. Solar Radio Flux Density ($F_{10.7}$)

The 10.7 cm solar radio flux density ($F_{10.7}$) is a widely used standard index and is one of the most operationally useful indicators of solar activity. Solar emissions around 10.7 cm wavelength are very sensitive to the conditions in the upper chromosphere and at the base of the corona (Tapping, 2013). Also, the radio flux at this wavelength easily penetrates clouds, so this index can be generated reliably from ground observations, regardless of sky conditions. Statistical studies show that the solar radio flux density is proportional to the sunspot number (Johnson, 2011), which is why the $F_{10.7}$ index has been adopted as a proxy for the solar activity. All observations presented here correspond to the period of solar minimum, during which there was relatively little variation in $F_{10.7}$ (Table 1). More particularly, the plot of $F_{10.7}$ indices (Figure 9) does not show any obvious difference between days with stalled versus emerging cross-polar jets. We made this plot of the $F_{10.7}$ index in order to check whether the differences in the stalling behavior that we do see had an obvious connection to the $F_{10.7}$ index prevailing on those days. However, because all our study days correspond to similar (and very low) values of $F_{10.7}$, there was not enough variation in the index to establish a correlation with the stalling of the cross-polar jet. Nevertheless, the statistical prevalence of stalling during solar minimum periods in our larger data set (as shown in Table 2) suggests that $F_{10.7}$ is indeed an important parameter.

3.4. Planetary K_p Indices on the Observation Days

Geomagnetic activity is routinely quantified by measuring disturbance levels in the geomagnetic field using ground-based magnetometers. For the location of our observations the auroral electrojet index (AE) and the three-hour planetary index, K_p (Thomsen, 2004) are both useful indices. While the auroral electrojet index (AE) does focus specifically on auroral latitudes, the longitudinal spacing of the observatories means that it is not sufficiently local to Alaska to offer a significant benefit for this study relative to the considerably more convenient planetary K_p index. Planetary K_p indices range from 0 to 9 and are derived from the maximum fluctuation in the geomagnetic field, at a number of largely mid-latitude and sub-auroral observatories, relative to a quiet day. K_p values for each of our study days are presented in Table 1. On none of the observation days presented in this study did the K_p index exceed 5, indicating generally quiet to moderately active conditions. On the days when the cross-polar jets stalled, the average K_p value was between 1 and 2 (Figure 10). By contrast, the average K_p value corresponding to the cross-polar jets emerging from the polar cap was between 3 and 4 (Figure 10).

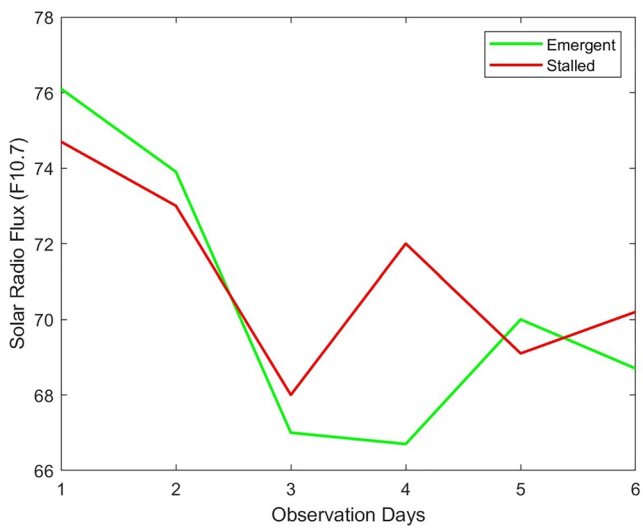

Figure 9. $F_{10.7}$ indices corresponding to emergent and stalled cross-polar jets. Here we have plotted the observation days along the x-axis, where the numbers 1 through 6 are assigned for six days of observation, and the y-axis shows the corresponding $F_{10.7}$ values. Note that the ordering of days on the x-axis of this plot is not significant.

3.5. Poker Flat Magnetic Data

In order to characterize the magnetic disturbances in the immediate region of our observations, Figures 11 and 12 show time series of the magnetic H-component measured at Poker Flat, Alaska. Figure 11 presents data for the emergent days, and Figure 12 shows corresponding data for the stalled days. As seen from these plots, perturbations in

Table 1
Geophysical Indices for the Observation Days

Cross-polar jet	Date	$F_{10.7}$	Three hourly K_p-indices in the period of the day (hrs)							
			0–3	3–6	6–9	9–12	12–15	15–18	18–21	21–24
Stalled	January 30, 2017	74.7	1	1	1	1	2	2	1	3
	February 15, 2017	73.0	0	0	1	1	1	1	1	1
	January 8, 2018	68.0	0	0	3	1	4	3	2	2
	February 5, 2018	72.0	3	2	2	2	3	2	1	1
	January 4, 2019	69.1	1	1	1	2	2	3	3	3
	January 24, 2019	70.2	4	3	4	2	1	3	4	5
Emergent	January 18, 2017	76.1	1	3	3	3	3	4	4	4
	February 1, 2017	73.9	5	4	3	3	4	5	3	5
	December 28, 2018	67.0	4	4	5	3	4	3	4	3
	December 29, 2018	66.7	3	3	3	2	3	2	2	2
	February 1, 2019	70.0	3	4	3	2	3	3	3	4
	March 1, 2019	68.7	4	5	3	3	3	4	4	4

Note. Solar $F_{10.7}$ data were taken from https://www.spaceweather.gc.ca/solarflux/sx-5-en.php.

the magnetometer data were typically larger during the nights when the cross-polar jets emerged from the polar cap and spilled equatorward on the nightside (Figure 11) compared to the relatively quiet nights associated with the stalling of the winds (Figure 12).

3.6. Poker Flat Keograms

Auroral activity at four wavelengths is summarized for two example nights by Figures 13 and 14. These figures use the "keogram" format originally introduced by Eather and Mende (1981). These plots show brightness as a function of time for auroral emissions observed within a narrow strip of sky aligned along the geomagnetic meridian passing through Poker Flat. The horizontal axis represents time and the vertical axes indicate look-angle along the field-of-view strip, with an angle of 0^o corresponding to the instrument viewing the horizon toward the magnetic north. Angles of 90^o and 180^o correspond to viewing the zenith and toward the south horizon respectively. The colors in the plot depict the brightness in units of Rayleighs of airglow/auroral emissions for wavelengths of 557.7, 427.8, 486.1, and 630.0 nm, according to the scale bars shown at the right. Figure 13 indicates high airglow/auroral emission brightness at 630.0 nm and multiple breakup events occurred during the night of January 18, 2017. This and other active nights correspond to the cross-polar jet passing over Alaska and spilling equatorward. By contrast, Figure 14 indicates that January 30, 2017 was a relatively quiet night with fainter and less active auroral forms that remained mostly poleward of Poker Flat. The cross-polar jet was observed to stall on this and other nights of quiet auroral activity.

3.7. Interplanetary Magnetic Field (IMF) Condition and Epsilon Parameter

The IMF carried by the solar wind has been known for decades to have a significant influence on energy and momentum transfer from the solar wind into the Earth's magnetosphere-ionosphere-thermosphere (MIT) system. Energy and momentum deposition into the neutral thermosphere in the auroral region changes the global circulation and triggers ionospheric/atmospheric disturbances (Zhang et al., 2019). However, the observed IMF conditions (Figures 15 and 16) do not show any obvious correlation with emergence or stalling of the cross-polar jet, at least for the days that we focus on in this study.

Table 2
Table Showing the Fraction of Days When the Cross-Polar Jet Get Stalled or Emerged Across Alaska in Different Years and Months of the Year

Months	State of the cross-polar jet	Number of observation days							Total days by months	Fraction of days by month
		Years								
		2013	2014	2015	2016	2017	2018	2019		
January	Emerged	8	0	7	14	5	4	4	42	0.70
	Stalled	2	0	0	0	5	5	6	18	0.30
February	Emerged	7	0	14	21	4	1	9	56	0.747
	Stalled	6	0	1	0	6	4	2	19	0.25
March	Emerged	19	0	3	14	12	8	21	77	0.856
	Stalled	1	0	1	1	4	5	1	13	0.144
April	Emerged	8	0	0	7	0	8	17	40	0.816
	Stalled	1	0	0	1	0	7	0	9	0.184
August	Emerged	6	0	0	0	4	0	0	10	0.714
	Stalled	1	0	0	0	3	0	0	4	0.286
September	Emerged	15	0	0	11	9	8	6	49	0.961
	Stalled	1	0	0	0	0	1	0	2	0.039
October	Emerged	9	16	0	26	0	8	14	73	0.901
	Stalled	2	1	0	0	0	5	0	8	0.099
November	Emerged	8	19	9	13	12	14	7	82	0.943
	Stalled	0	0	0	1	1	2	1	5	0.057
December	Emerged	18	10	2	7	14	7	6	64	0.842
	Stalled	0	1	0	2	2	5	2	12	0.158
Total days by years	Emerged	98	45	35	113	60	58	84	493	0.846
	Stalled	14	2	2	5	21	34	12	90	0.154
Fraction by years	Emerged	0.875	0.957	0.946	0.958	0.741	0.630	0.875		
	Stalled	0.125	0.043	0.054	0.042	0.259	0.370	0.125		

Akasofu's epsilon parameter, ε (Perreault & Akasofu, 1978), is thought to be another useful proxy for the amount of solar wind power that is coupled to the Earth's MIT system. A fraction of the coupled energy would be dissipated through driving winds in the thermosphere. ε depends on the solar wind speed, v, the IMF intensity, B, and the so-called clock angle, θ, of the IMF orientation perpendicular to the Sun-Earth line that is, $\tan\theta = B_y/B_z$. In SI units,

$$\varepsilon = (4\pi/\mu_0)vB^2 \sin^4(\theta/2)l_0^2$$

where $\mu_0 = 4\pi \times 10^{-7}$H/m and l_0 is an empirically determined scale factor ($l_0 = 7R_E$) having the dimension of length (Koskinen & Tanskanen, 2002). It would be reasonable to expect that the epsilon parameter would have some correlation with the behavior of the cross-polar jet. The strength of the high-latitude ion convection circulation is typically parameterized by the cross-polar-cap potential drop, which increases as the epsilon parameter increases. These conditions are also typically associated with increased auroral precipitation, and hence aurorally enhanced F-region plasma densities. These two mechanisms (faster convection of denser plasma) would be expected to increase ion-neutral momentum coupling and, ultimately, drive a stronger cross-polar wind jet. However, at least for our 12 study days, there is not any obvious relationship between the epsilon parameter and the stalling or emergence of the cross-polar jet (Figures 15 and 16). In particular, a low value for epsilon does not guarantee that the cross-polar jet will fail to emerge from the polar cap.

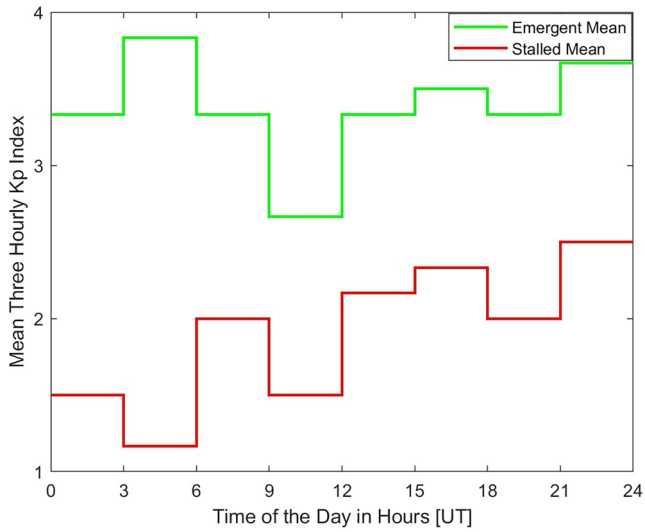

Figure 10. Mean K_p indices versus UT, for days of stalled (red) and emergent (green) cross-polar jets. For both data sets, flat line in the plot shows the mean of the K_p indices for all six days of observation within the given three hour window.

3.8. Comparison With Model Results

Observations presented here indicate that stalling of the cross-polar jet can occur over Alaska and that the characteristic length scale for this stalling can be as short as ~200 km. This is very abrupt in the context of the existing understanding of the length and time scales associated with *F*-region neutral flow features. The data thus show that stalling is a highly localized feature compared to the large scale meteorology of the thermosphere in general, and to the cross-polar jet in particular. To illustrate this, we have compared our results with predictions of cross-polar jet behavior from the TIEGCM (Richmond et al., 1992). TIEGCM is a global 3-D numerical model that simulates the coupled thermosphere-ionosphere system with 2.5×2.5 degrees latitude-longitude spatial resolution and time step of 120 s. As TIEGCM model runs make use of the time history of the solar and geophysical indices, geophysical conditions in the model runs were matched to those present on the observation days. Both the TIEGCM model (Figure 17) and the SDI data agree that the wind would not have stalled suddenly above Alaska on February 1, 2017. The model output shows the cross-polar jet flow spilling far south in the midnight sector, only slowing gradually, and reaching latitudes near southern California. However, although our data did not show sudden stalling on this day, observations do show that the jet was clearly slowing as it passed over Alaska, more strongly than suggested by the model. The Community Coordinated Modeling Center (CCMC) model predictions are rather generic, and not driven by specific local fields observed over Alaska. The SDI saw a clear stalling of the cross-polar jet on the night of February 15, 2017, but the model output is again inconsistent with observations. Even on this day, the model output showed that the cross-polar jet would extend far south of Alaska in the midnight sector (Figure 18). Our data, by contrast, shows the jet clearly present over northern Alaska, but stalling abruptly at approximately the latitude of Poker Flat. Note that the days for which we requested model runs (February 1, 2017 and February 15, 2017) were randomly chosen from this study's list of emergent and stalled days.

We have also examined the behavior of the cross-polar jet predicted by the Horizontal Wind Model (HWM14) (Drob et al., 2008, 2015; Hedin et al., 1988, 1991, 1996) for selected days and a range of A_p index. HWM14 uses vector spherical harmonic functions for wind fitting, and so its spatial resolution is limited by the order of harmonics. For HWM14, the maximum orders in latitude, longitude, and local time are 8, 2, and 3 respectively (Drob et al., 2015). Because HWM14 is a purely index-driven empirical model, it does not respond very specifically to conditions on a given day. Thus, for this study, it is more reasonable to show the range of possible model behaviors rather than modeling each study day individually. Although HWM14 is a climatological model, it can resolve the differences between quiet and active days and respond accordingly on time scales comparable to the three hour cadence at which the A_p index is resolved. Stalling of the cross-polar jet appears to be a repeatable climatological feature, and thus should be captured by the empirical data used to assemble the HWM14 model. The most recent formulation, HWM14, includes a significant amount of our own SDI data from Poker Flat. Even so, Figure 19 does not show the stalling over Alaska that we see with the SDI, presumably because this feature is smoothed out by the data assimilation and climatological fitting of spherical harmonic basis functions. While it is not too surprising that HWM14 cannot resolve the sudden stalling of the jet that we observed with the SDI, we might still anticipate that it would predict a significant difference in the midnight sector wind fields between the emergent and stalled days. Its failure to do so suggests that stalling is an insufficiently common and repeatable occurrence for it to be captured clearly by the model fitting process.

Overall, neither HWM14 nor TIEGCM appeared to be able to reproduce this wind feature at the length scales that we have seen. We infer that neither model has an adequate resolution to depict small scale processes such as the stalling of the cross-polar jet.

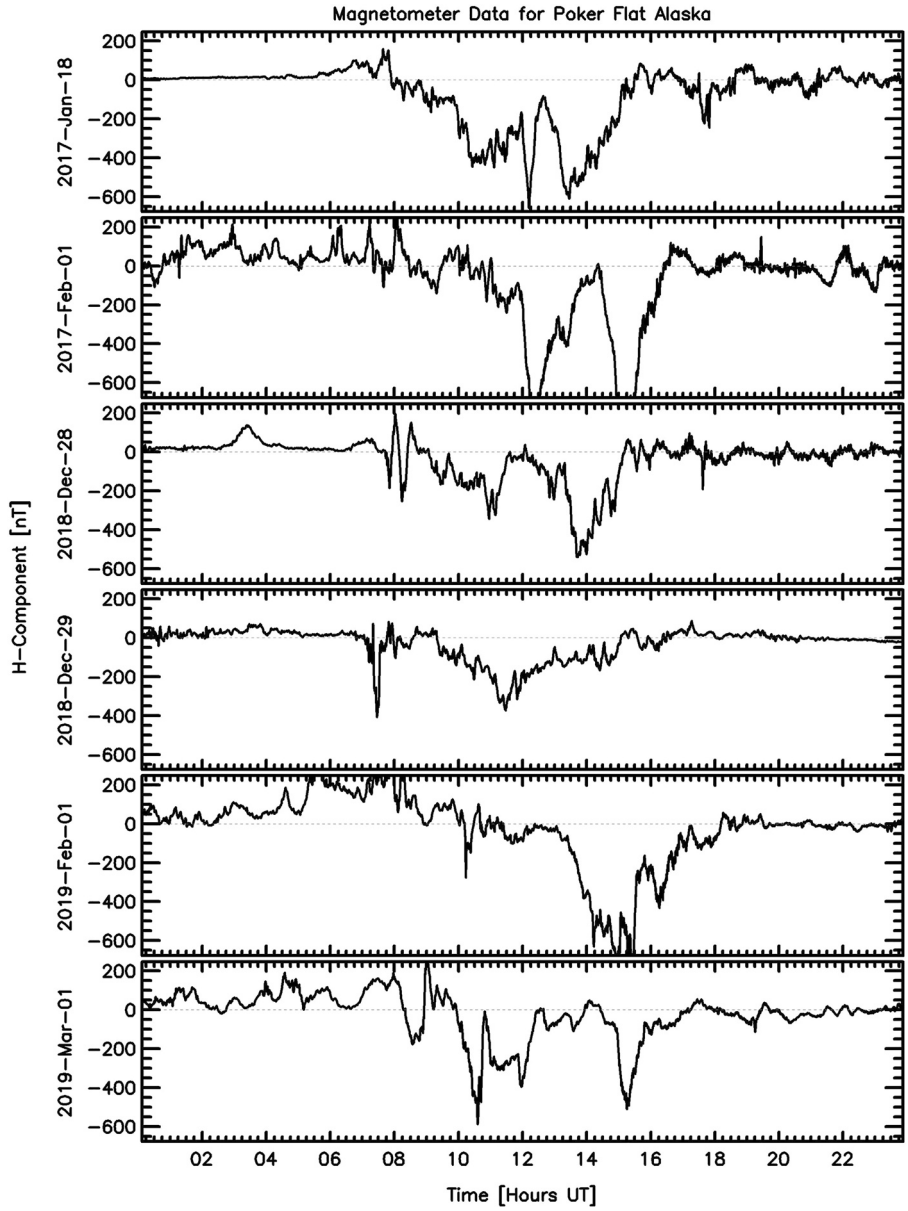

Figure 11. Time series of ground-based measurements of the magnetic H-component on days with emergent events, as observed from Poker Flat, Alaska.

3.9. Occurrence Frequencies

In addition to the days we discussed above, we visually examined a full seven years of SDI data in order to tabulate the simple occurrence frequency of both stalled and emergent cross-polar jets. In examining these data we noted, as expected, that there were many nights when it was cloudy, along with nights when the instrument was not working well for various reasons. There are also nights when the wind behavior was reasonably complex and not easily classified into a clear instance of either a stalled or emergent cross-polar jet. Also, there were a small number of instances of conditions so quiet that the cross-polar jet did not even reach into the field of view of our instrument at Poker Flat, Alaska. On those quiet days, the airglow and the auroral signal was weak, and the wind pattern was not amenable for classification into two simple categories of stalled versus emergent behavior. Overall, we therefore excluded any days when we could not clearly classify the behavior of the jet. The remaining nights were

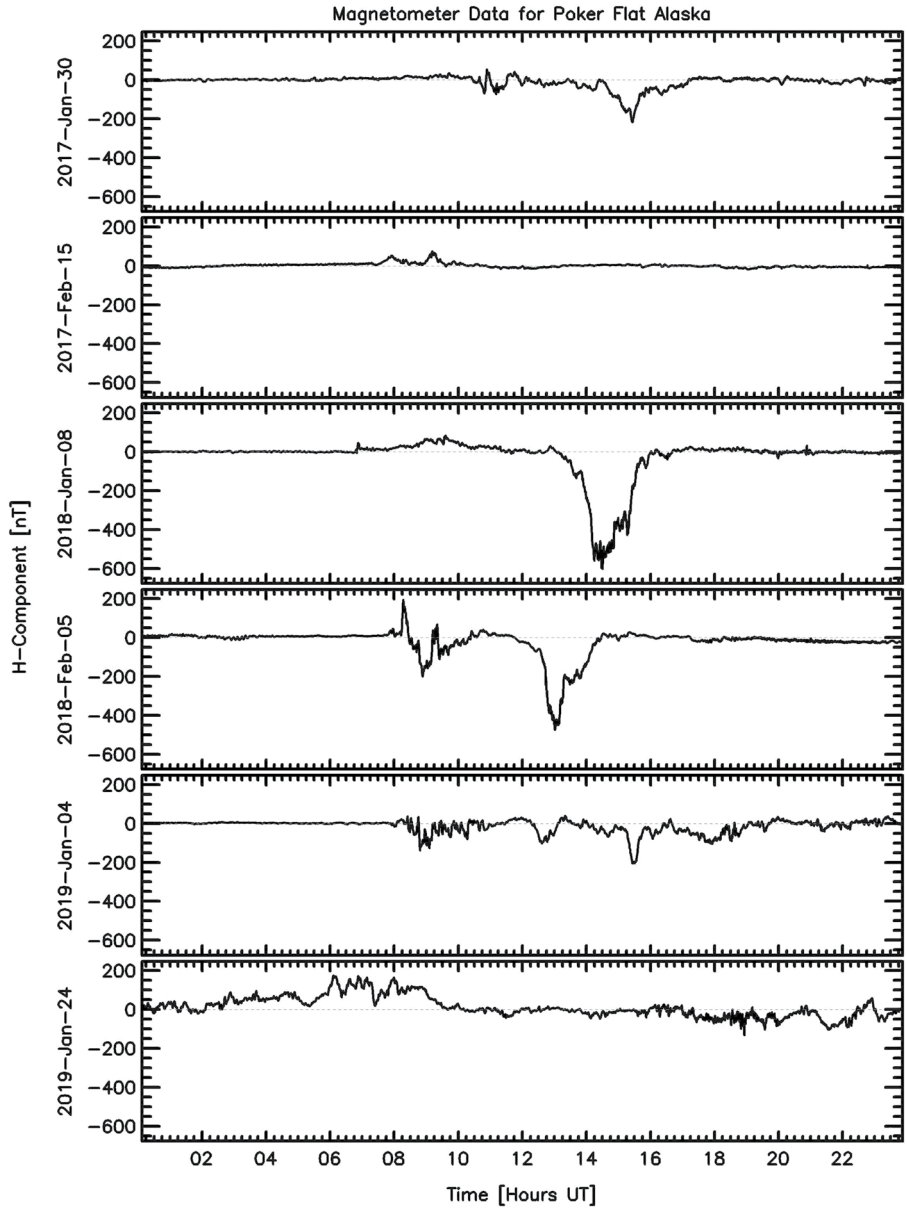

Figure 12. Magnetometer data for the stalled events from Poker Flat, Alaska, in the same format as Figure 11.

then manually characterized based on a qualitative visual assessment into categories corresponding to either the emergence or stalling of the cross-polar jet, as shown in Table 2. Results show that the emergence of the cross-polar jet was by far the dominant scenario (e.g., ~88% in the year 2014 and ~63% in the year 2018). By contrast, although stalling is not a frequent behavior, it is also not particularly unusual. As shown in Table 2, stalling did appear to be more common at solar minimum. For example, ~26% in the year 2017 and ~37% in the year 2018, which contrasts with a solar maximum when, for example, it occurred ~12.5% of the time in the year 2013 and ~4.26% in the year 2014. It must once again be emphasized that the results appearing in Table 2 only apply to nights when the cross-polar jet feature was easily recognizable in the data and we could distinguish whether or not it manifested the stalling phenomenon.

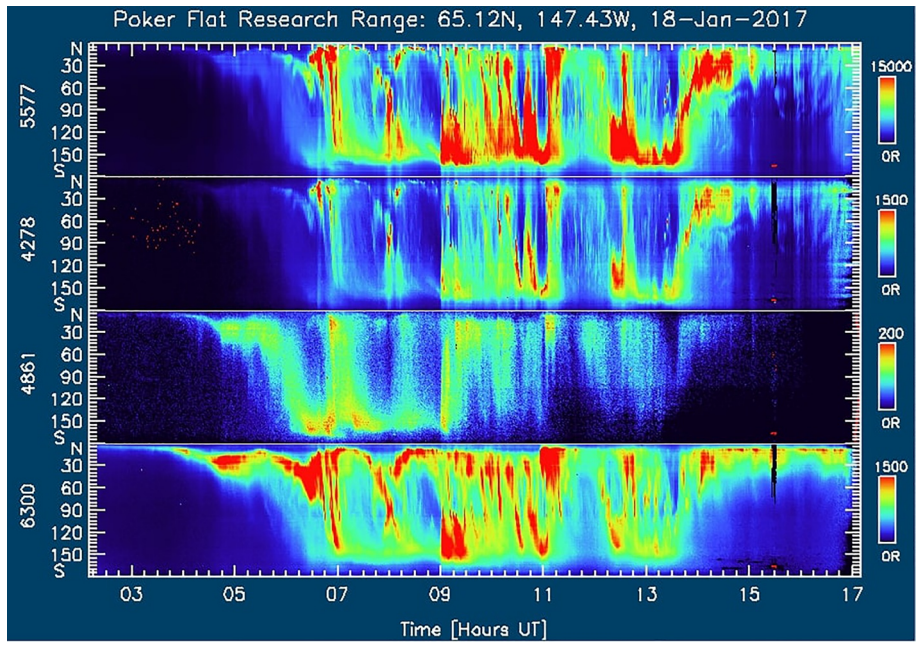

Figure 13. Keograms of auroral brightness recorded using a meridian spectrograph instrument at Poker Flat, Alaska on January 18, 2017. On this day the cross-polar jet emerged in the midnight sector. The four sub-panels show the time history of emission brightness measured along the geomagnetic meridian, for wavelengths of 557.7, 427.8, 486.1, and 630.0 nm. These wavelengths are emitted by O, N2+, H, and O respectively.

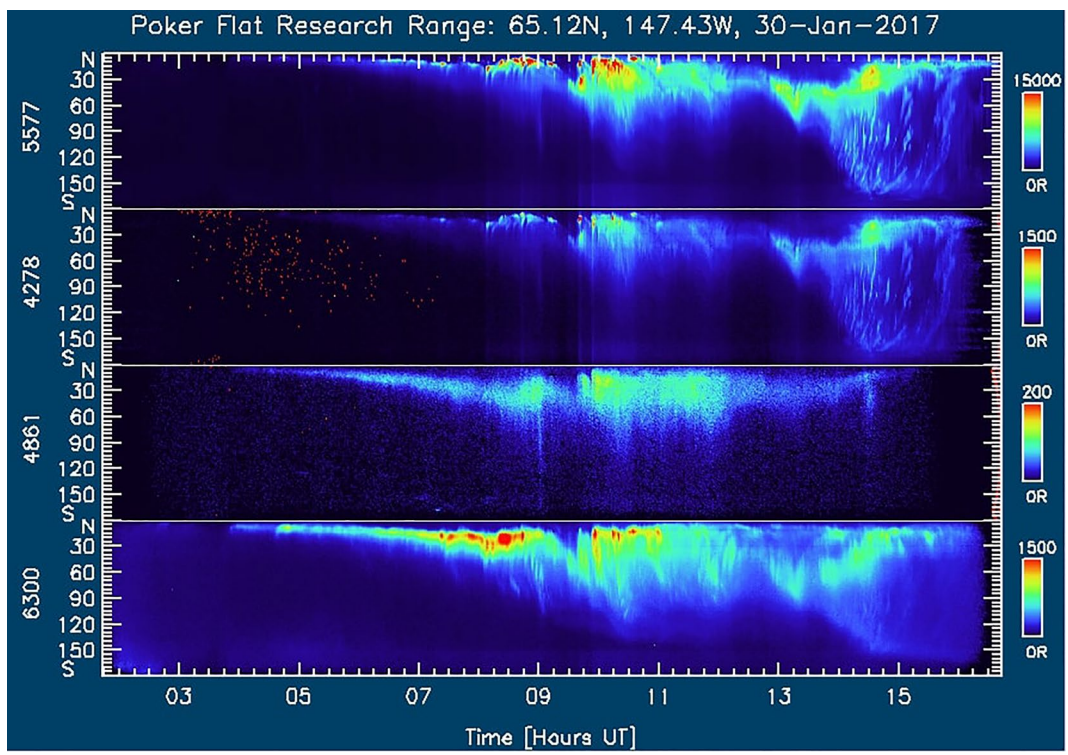

Figure 14. Same as Figure 13 but for the day of January 30, 2017. On this day the cross-polar jet stalled over Poker Flat, Alaska.

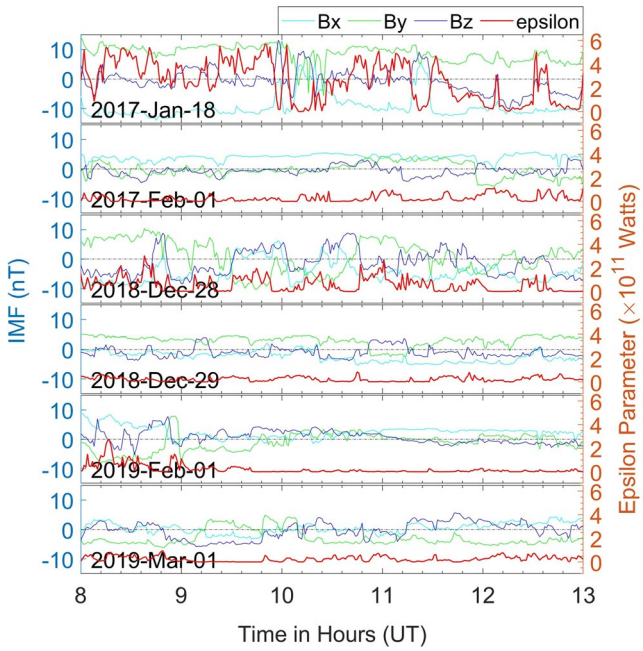

Figure 15. Interplanetary magnetic field components and Akasofu's epsilon parameter in the midnight sector corresponding to the days when the cross-polar jet emerged in the midnight sector.

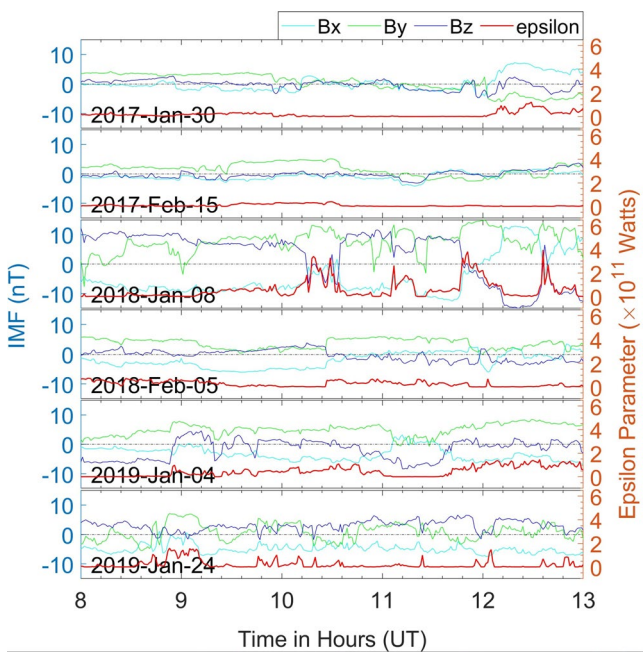

Figure 16. Interplanetary magnetic field components and Akasofu's epsilon parameter in the midnight sector corresponding to the days when the cross-polar jet stalled.

4. Discussion

A common approach for studying thermospheric winds is to calculate climatological average flows based on a large number of separate observations. However, in this case, the location of the stalling varies day-to-day by more in latitude than the latitudinal distance over which the stalling occurs. This means that large-scale averaging is not appropriate in this case, because it would "washout" the sharp stalling feature of interest. Thus, this particular research is instead presented via a small set of case studies. The study days were examined visually and largely qualitatively, as is appropriate for a complex 2D flow feature such as the cross-polar jet.

Theory and first-principle models suggest that strong modulation of the upper thermospheric winds should be unlikely to occur at length scales smaller than ~500 km (Killeen & Roble, 1988; Killeen et al., 1988; Smith et al., 1988). By contrast, what we actually observed on individual study days is considerably more structured behavior than these expectations. These results thus suggest that current modeling does not adequately describe coupling processes occurring at small scales.

The main topic of interest in this study is thus not simply instances of limited equatorward penetration of the cross-polar jet in the midnight sector. Rather, it is the observed abrupt nature of the stalling, which implies more than a passive attenuation of the flow as it spills out from the polar cap. This behavior would seem to require some highly localized active forcing to inhibit the flow so suddenly. Figure 20 offers a clue what this process might involve. On this particular night, stalling did occur, but only for a brief period (around 10:30 UT to 11:00 UT) that happened to coincide spatially and temporally with a brightening of the aurora (as indicated by green hues in the plotted panels). The aurora itself appears to have undergone a "mini breakup" as it brightened at this time. This behavior strongly suggests that aurora plays a role in the mechanism that allows the stalling to occur so abruptly.

Understanding what drives the abrupt stalling is important because processes occurring at the scales examined here could potentially degrade the accuracy of spacecraft orbital positions, ionospheric storm modeling, or understanding of any process involving thermospheric wind transport. This is particularly true for the cross-polar jet, due to its dominant role in transporting air parcels across the polar cap to auroral latitudes in the midnight sector and, during storm times, even to sub-auroral and mid-latitudes (Fuller-Rowell, 2011; Prölss, 1997). Results here show that the latitudinal extent of nightside equatorward transport by this feature can be far more limited than expected, with major implications for the understanding of the consequences of this transport. For example, air parcels that have been chemically modified by the auroral precipitation may reach mid-latitude regions less easily and frequently than previously expected.

In response to a concern raised during review, we considered the possibility that stalling occurs during all or most levels of geophysical activity, albeit possibly at locations that, under active conditions, are located too far equatorward to be observed from Poker Flat. For example, Figure 21 shows observations in the night of September 4, 2011, when stalling was observed from the HAARP site at Gakona, Alaska, but no stalling was de-

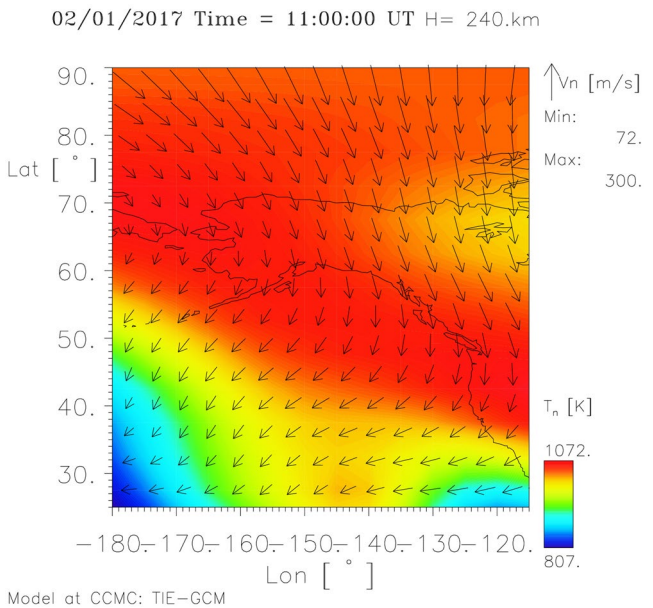

Figure 17. Thermosphere Ionosphere Electrodynamics General Circulation Model wind field from the Community Coordinated Modeling Center (CCMC) for the day of February 1, 2017 at 240 km altitude. This result was obtained using Weimer electric field model run using the time history of solar wind inputs and $F_{10.7}$ index. The black arrow vectors represent the thermospheric neutral wind speed and direction as implied by the scale arrow at the top right of the figure. Blue through red colors show the neutral temperature as indicated by the color scale bar at bottom right of the plot.

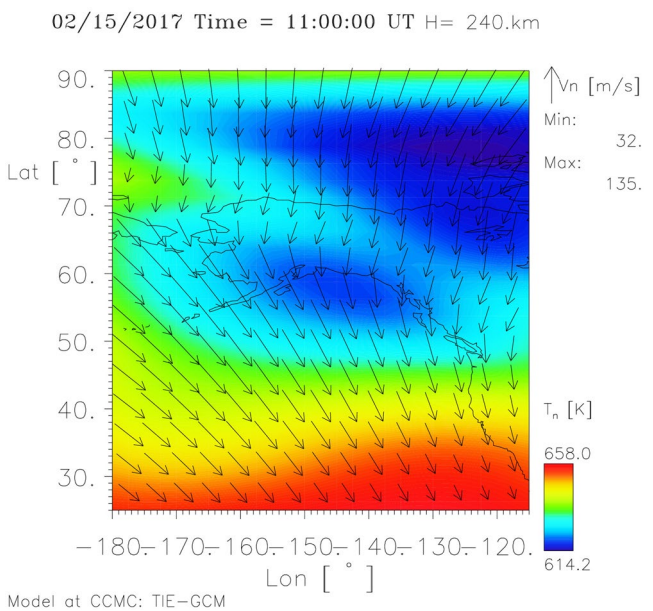

Figure 18. Thermosphere Ionosphere Electrodynamics General Circulation Model wind field from the Community Coordinated Modeling Center (CCMC) for the day of February 15, 2017 at 240 km altitude. In generating output for this event the model used the Weimer electric field and the time history of solar wind inputs and $F_{10.7}$ index. The arrow vectors represent the neutral wind speed and the blue through red colors represent the neutral temperature.

tected by Poker SDI. However, we found no instances of stalling observed from Gakona during the roughly solar maximum period of 2012–2014, despite the more equatorward location of this observatory. These data do not exclude the possibility that, under active conditions, stalling may occur very much further equatorward than can be observed from either Poker Flat or Gakona. Rather, they establish that if such stalling does occur, it must be displaced so much further equatorward that it is outside the field of view of even the SDI at Gakona.

5. Conclusions

This study was motivated by data acquired by the SDI at Poker Flat showing that, somewhat to our surprise, the cross-polar jet did not always flow smoothly equatorward around midnight as we expected; rather we observed instances of abrupt and unexpected stalling. This study characterized the stalling feature, but we have not yet investigated the physical mechanisms driving the stalling. Stalling was visually and qualitatively inspected and its correlation with other space weather drivers was studied. Although there was no obvious correlation with $F_{10.7}$ within the 12 sample days selected for case studies, results of a qualitative visual inspection of seven years of data show that the factor that is most significant in determining whether or not the stalling occurs is the solar activity; stalling was more likely to occur during solar minimum than at solar maximum. Stalling appeared to occur over Alaska more readily during the deep northern hemisphere winter. This is presumably because of the lack of sunlight and resulting low ion densities meaning that there is less coupling to the ion convection pattern and therefore the wind can stall more easily. Another major factor determining the likelihood of stalling of the cross-polar jet was magnetic activity. The jet was less likely to stall on nights when auroral and magnetic conditions had been active for many hours so that ion drag had established a stronger and more dominant cross-polar jet. Somewhat in contrast to this, we also saw instances where stalling appeared to be caused by a brief brightening of the aurora around midnight, on nights when it had previously been quiet.

Our data were unable to establish an explicit correlation between the 10.7 cm solar radio flux density and the stalling behavior of the cross-polar jet, at least for our 12 focused study days. This is because there was not enough difference in $F_{10.7}$ values between the selected days of stalled versus emergent jets to resolve such an effect. Nevertheless, the statistics of stalling occurrence compiled from our larger data set do show that stalling is most common during solar minimum, suggesting that the difference between the maximum and minimum solar activity does have a strong influence. In addition, IMF conditions and the epsilon parameter only had a minor influence on the stalling of the cross-polar jet. Although the emergence or stalling of the cross-polar jet occasionally appears to correlate with the parameters like $F_{10.7}$, K_p, geomagnetic conditions, IMF, and epsilon parameter, none of them is by itself enough to guarantee that the cross-polar jet would either stall or emerge. That is to say, there were days with low solar and geomagnetic activity when the cross-polar jet emerged and there were active days when the jet stalled.

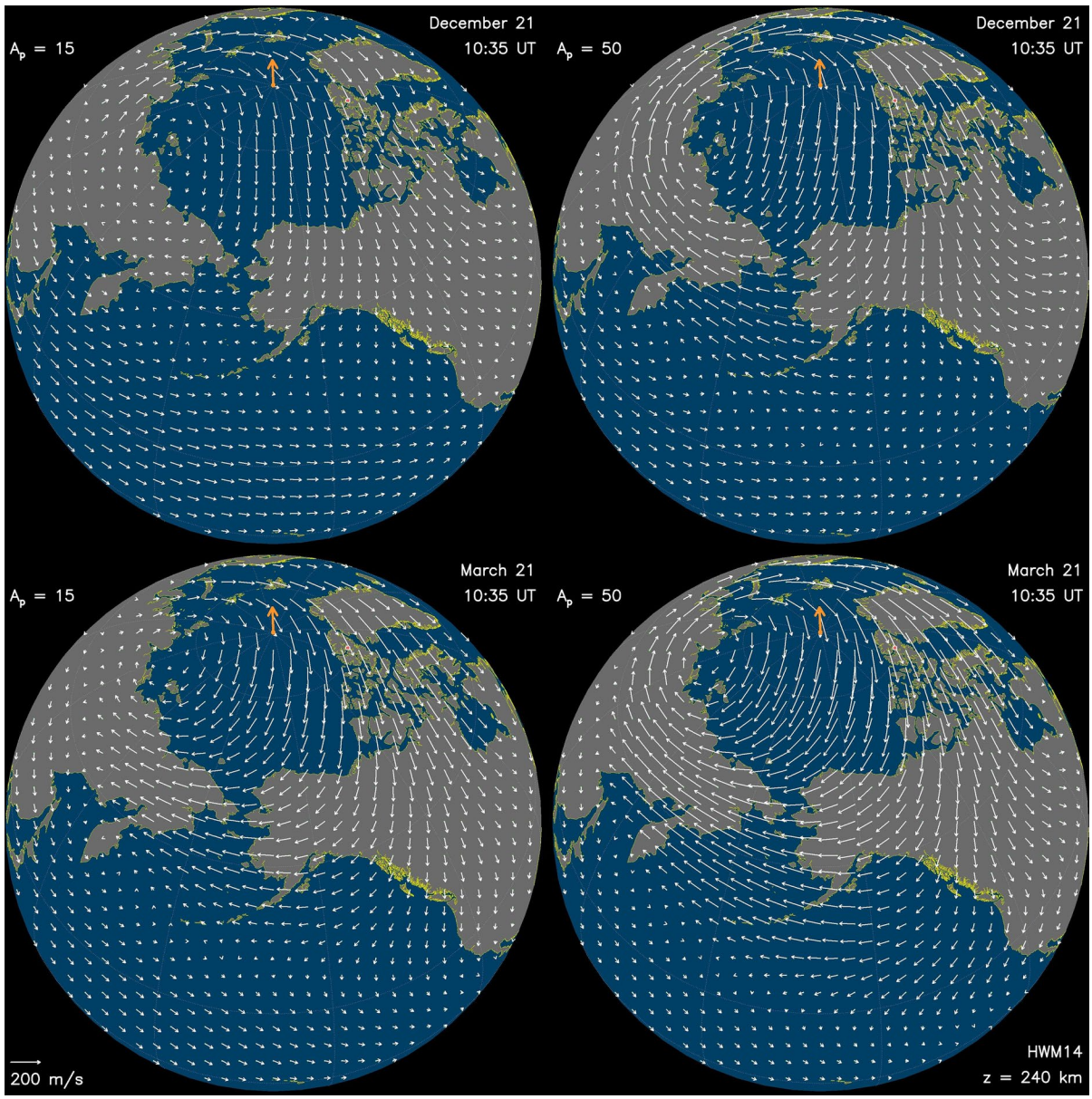

Figure 19. Wind fields over the northern hemisphere predicted by the HWM14 model for December solstice (top row) and March equinox (bottom row). Two different levels of magnetic activity are shown, as indicated by the labels for each panel. The orange arrow in each plot panel depicts the great circle bearing toward the sub-solar point.

We have also looked at TIEGCM and HWM14 models and found that they are unable to reproduce the stalling of the cross-polar jet observed on the scale that we saw. Note that HWM14 itself is based on observations including SDI data. Clearly, the observed behavior of the cross-polar jet is not well predicted at the moment. This could cause problems because the cross-polar jet is a large scale feature that can influence any technological system that is affected by conditions in the thermosphere. For example, spacecraft orbital predictions may need to account for this rather more complex behavior of the cross-polar jet than is described by the currently prevailing paradigm.

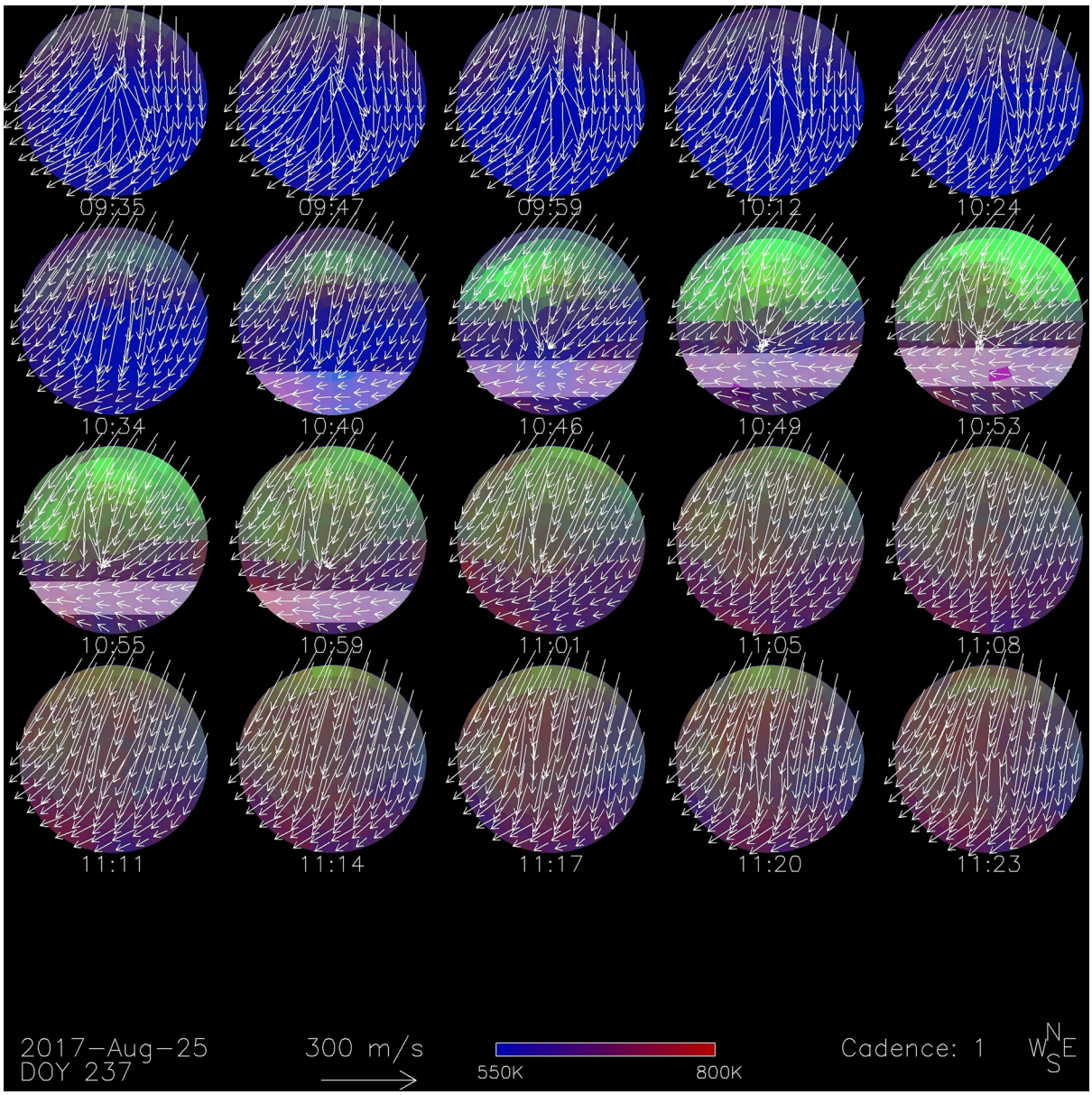

Figure 20. Vector wind plots from around magnetic midnight on August 25, 2017. Each circle is showing Scanning Doppler Imager measurements of temperature, 630.0 nm brightness, and vector wind field at the indicated UT time. White arrows represent wind direction and speed, as indicated by the length scale arrow. Green hues depict airglow/auroral intensity and the blue through red colors show Doppler temperatures according to the color scale bar at the bottom. Note that unlike Figures 1–5, geomagnetic directions shown here are fixed with respect to universal time. However, since these data are from around magnetic midnight, orientations in this figure are similar to those of Figures 2–5. Stalling of the cross-polar jet is highlighted by a band of modified color, generally pink, on the lower half of four frames in the second row and first two frames in the third row. On this day the 10.7 cm solar radio flux index ($F_{10.7}$) was 82.5. Geomagnetic activity was quiet to unsettled, as indicated by the K_p index, which varied in the range 2–3.

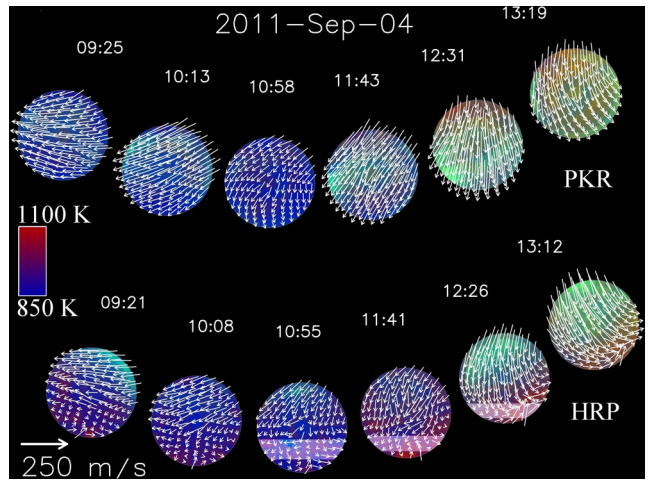

Figure 21. Midnight sector dial plot for the night of September 4, 2011 as observed from Poker Flat (PKR) and Gakona (HRP) Alaska. On this night the cross-polar wind jet stalled over Gakona however it did not stall within the field-of-view of our Poker instrument. Blue through red colors represent temperature derived from Doppler width of the 630 nm spectra as indicated by the color bar on the left side of the plot. Green hues depict the auroral/airglow emission brightness at 630.0 nm in arbitrary units. Regions of stalling seen in the HRP data have been highlighted using pink-colored shading at times 10:55 UT, 11:41 UT, and 12:26 UT (lower half of three circles in the bottom row).

Data Availability Statement

The version of HWM14 that we used was derived from the executable files provided by the US Naval Research Laboratory. The original SDI data can be freely downloaded from the SDI server at http://sdi_server.gi.alaska.edu/sdi_web_plots. Solar $F_{10.7}$ data were taken from https://www.spaceweather.gc.ca/forecast-prevision/solar-solaire/solarflux/sx-5-flux-en.php.

Acknowledgments
This research was supported by NSF award number 1452333, "CEDAR: High-resolution Multistatic Mapping of Small-Scale Flow Structures in Earth's Auroral Thermosphere." We would like to thank the CCMC for providing the TIEGCM model output. We would like to acknowledge D. Hampton for providing the magnetometer data (URL: https://www.gi.alaska.edu/monitors/magnetometer/archive) and the Meridian Spectrograph data (URL: http://optics.gi.alaska.edu/optics/archive).

References

Anderson, C., Conde, M., & McHarg, M. (2012a). Neutral thermospheric dynamics observed with two scanning doppler imagers: 1. monostatic and bistatic winds. *Journal of Geophysical Research*, *117*(A3), A03304. https://doi.org/10.1029/2011ja017041

Anderson, C., Conde, M., & McHarg, M. (2012b). Neutral thermospheric dynamics observed with two scanning doppler imagers: 2. vertical winds. *Journal of Geophysical Research*, *117*(A3), A03305. https://doi.org/10.1029/2011ja017157

Anderson, C., Conde, M., & McHarg, M. (2012c). Neutral thermospheric dynamics observed with two scanning doppler imagers: 3. horizontal wind gradients. *Journal of Geophysical Research*, *117*(A5), A05311. https://doi.org/10.1029/2011ja017471

Banks, P., & Kockarts, G. (1973). Chapter 8 - Photodissociation. In P. Banks, & G. Kockarts (Eds.), *Aeronomy* (pp. 167–183). Academic Press. https://doi.org/10.1016/B978-0-12-077801-0.50013-5

Bates, D. (1978). Forbidden oxygen and nitrogen lines in the nightglow. *Planetary and Space Science*, *26*(10), 897–912. https://doi.org/10.1016/0032-0633(78)90073-9

Conde, M., Bristow, W., Hampton, D., & Elliott, J. (2018). Multiinstrument studies of thermospheric weather above Alaska. *Journal of Geophysical Research: Space Physics*, *123*(11), 9836–9861. https://doi.org/10.1029/2018ja025806

Conde, M., Craven, J., Immel, T., Hoch, E., Stenbaek-Nielsen, H., Hallinan, T., et al. (2001). Assimilated observations of thermospheric winds, the aurora, and ionospheric currents over Alaska. *Journal of Geophysical Research*, *106*(A6), 10493–10508. https://doi.org/10.1029/2000ja000135

Conde, M., & Smith, R. (1995). Mapping thermospheric winds in the auroral zone. *Geophysical Research Letters*, *22*(22), 3019–3022. https://doi.org/10.1029/95gl02437

Conde, M., & Smith, R. (1997). Phase compensation of a separation scanned, all-sky imaging fabry–perot spectrometer for auroral studies. *Applied Optics*, *36*(22), 5441–5450. https://doi.org/10.1364/ao.36.005441

Conde, M., & Smith, R. (1998). Spatial structure in the thermospheric horizontal wind above poker flat, Alaska, during solar minimum. *Journal of Geophysical Research*, *103*(A5), 9449–9471. https://doi.org/10.1029/97ja03331

de Meneses, F., Muralikrishna, P., & Clemesha, B. (2008). Height profiles of oi 630 nm and oi 557.7 nm airglow intensities measured via rocket-borne photometers and estimated using electron density data: A comparison. *Geofisica Internacional*, *47*(3), 161–166. https://doi.org/10.22201/igeof.00167169p.2008.47.3.76

Dhadly, M. S., Emmert, J. T., Drob, D. P., Conde, M. G., Doornbos, E., Shepherd, G. G., et al. (2018). Seasonal dependence of geomagnetic active-time northern high-latitude upper thermospheric winds. *Journal of Geophysical Research: Space Physics*, *123*(1), 739–754. https://doi.org/10.1002/2017ja024715

Drob, D., Emmert, J., Crowley, G., Picone, J., Shepherd, G., Skinner, W., et al. (2008). An empirical model of the Earth's horizontal wind fields: Hwm07. *Journal of Geophysical Research*, *113*(A12), A12304. https://doi.org/10.1029/2008ja013668

Drob, D., Emmert, J. T., Meriwether, J. W., Makela, J. J., Doornbos, E., Conde, M., et al. (2015). An update to the horizontal wind model (hwm): The quiet time thermosphere. *Earth and Space Science*, *2*(7), 301–319. https://doi.org/10.1002/2014ea000089

Eather, R., & Mende, S. (1981). Dayside aurora studies with a keogram camera, Antarct. *JUS*, *15*, 203–211.
Fuller-Rowell, T. J. (2011). Storm-time response of the thermosphere–ionosphere system. In *Aeronomy of the Earth's atmosphere and ionosphere* (pp. 419–435). Springer. https://doi.org/10.1007/978-94-007-0326-1_32
Hedin, A. E., Biondi, M., Burnside, R., Hernandez, G., Johnson, R., Killeen, T., et al. (1991). Revised global model of thermosphere winds using satellite and ground-based observations. *Journal of Geophysical Research*, *96*(A5), 7657–7688. https://doi.org/10.1029/91ja00251
Hedin, A. E., Fleming, E., Manson, A., Schmidlin, F., Avery, S., Clark, R., et al. (1996). Empirical wind model for the upper, middle and lower atmosphere. *Journal of Atmospheric and Terrestrial Physics*, *58*(13), 1421–1447. https://doi.org/10.1016/0021-9169(95)00122-0
Hedin, A. E., Spencer, N., & Killeen, T. (1988). Empirical global model of upper thermosphere winds based on atmosphere and dynamics explorer satellite data. *Journal of Geophysical Research*, *93*(A9), 9959–9978. https://doi.org/10.1029/ja093ia09p09959
Heelis, R., Lowell, J. K., & Spiro, R. W. (1982). A model of the high-latitude ionospheric convection pattern. *Journal of Geophysical Research*, *87*(A8), 6339–6345. https://doi.org/10.1029/ja087ia08p06339
Johnson, R. W. (2011). Power law relating 10.7 cm flux to sunspot number. *Astrophysics and Space Science*, *332*(1), 73–79. https://doi.org/10.1007/s10509-010-0500-1
Kelley, M., Jøroensen, T. S., & Mikkelsen, I. S. (1977). Thermospheric wind measurements in the polar region. *Journal of Atmospheric and Terrestrial Physics*, *39*(2), 211–219. https://doi.org/10.1016/0021-9169(77)90114-3
Killeen, T., Craven, J., Frank, L., Ponthieu, J.-J., Spencer, N., Heelis, R., et al. (1988). On the relationship between dynamics of the polar thermosphere and morphology of the aurora: Global-scale observations from dynamics explorers 1 and 2. *Journal of Geophysical Research*, *93*(A4), 2675–2692. https://doi.org/10.1029/ja093ia04p02675
Killeen, T., Hays, P., Spencer, N. W., & Wharton, L. (1982). Neutral winds in the polar thermosphere as measured from dynamics explorer. *Geophysical Research Letters*, *9*(9), 957–960. https://doi.org/10.1029/gl009i009p00957
Killeen, T., & Roble, R. (1984). An analysis of the high-latitude thermospheric wind pattern calculated by a thermospheric general circulation model: 1. momentum forcing. *Journal of Geophysical Research*, *89*(A9), 7509–7522. https://doi.org/10.1029/ja089ia09p07509
Killeen, T., & Roble, R. (1988). Thermosphere dynamics: Contributions from the first 5 years of the dynamics explorer program. *Reviews of Geophysics*, *26*(2), 329–367. https://doi.org/10.1029/rg026i002p00329
Koskinen, H. E., & Tanskanen, E. I. (2002). Magnetospheric energy budget and the epsilon parameter. *Journal of Geophysical Research*, *107*(A11), 1415. https://doi.org/10.1029/2002ja009283
Liuzzo, L., Ridley, A., Perlongo, N., Mitchell, E., Conde, M., Hampton, D., & Nicolls, M. (2015). High-latitude ionospheric drivers and their effects on wind patterns in the thermosphere. *Journal of Geophysical Research: Space Physics*, *120*(1), 715–735. https://doi.org/10.1002/2014ja020553
McCormac, F., Killeen, T., Nardi, B., & Smith, R. (1987). How close are ground-based fabry-perot thermospheric wind and temperature measurements to exospheric values? A simulation study. *Planetary and Space Science*, *35*(10), 1255–1265. https://doi.org/10.1016/0032-0633(87)90110-3
McGrath, W., & McGarvey, J. (1967). The production, deactivation and chemical reactions of o (1d) atoms. *Planetary and Space Science*, *15*(3), 427–455. https://doi.org/10.1016/0032-0633(67)90154-7
Meriwether, J., Heppner, J., Stolarik, J., & Wescott, E. (1973). Neutral winds above 200 km at high latitudes. *Journal of Geophysical Research*, *78*(28), 6643–6661. https://doi.org/10.1029/ja078i028p06643
Meriwether, J., Jr, Killeen, T., McCormac, F., Burns, A., & Roble, R. (1988). Thermospheric winds in the geomagnetic polar cap for solar minimum conditions. *Journal of Geophysical Research*, *93*(A7), 7478–7492. https://doi.org/10.1029/ja093ia07p07478
Perreault, P., & Akasofu, S. (1978). A study of geomagnetic storms. *Geophysical Journal International*, *54*(3), 547–573. https://doi.org/10.1111/j.1365-246x.1978.tb05494.x
Prölss, G. W. (1997). Magnetic storm associated perturbations of the upper atmosphere. *Magnetic storms*, *98*, 227–241. https://doi.org/10.1029/gm098p0227
Richmond, A., Ridley, E., & Roble, R. (1992). A thermosphere/ionosphere general circulation model with coupled electrodynamics. *Geophysical Research Letters*, *19*(6), 601–604. https://doi.org/10.1029/92gl00401
Roble, R. G., Dickinson, R., Ridley, E., Emery, B., Hays, P., Killeen, T., & Spencer, N. W. (1983). The high latitude circulation and temperature structure of the thermosphere near solstice. *Planetary and Space Science*, *31*(12), 1479–1499. https://doi.org/10.1016/0032-0633(83)90021-1
Slanger, T. G., & Copeland, R. A. (2003). Energetic oxygen in the upper atmosphere and the laboratory. *Chemical Reviews*, *103*(12), 4731–4766. https://doi.org/10.1021/cr0205311
Smith, R., Hernandez, G., Roble, R., Dyson, P., Conde, M., Crickmore, R., & Jarvis, M. (1998). Observation and simulations of winds and temperatures in the Antarctic thermosphere for August 2–10, 1992. *Journal of Geophysical Research*, *103*(A5), 9473–9480. https://doi.org/10.1029/97ja03336
Smith, R., Rees, D., & Stewart, R. (1988). Southern hemisphere thermospheric dynamics: A review. *Reviews of Geophysics*, *26*(3), 591–622. https://doi.org/10.1029/rg026i003p00591
Tapping, K. (2013). The 10.7 cm solar radio flux (f10. 7). *Space Weather*, *11*(7), 394–406. https://doi.org/10.1002/swe.20064
Thomsen, M. (2004). Why kp is such a good measure of magnetospheric convection. *Space Weather*, *2*(11), 1–10. https://doi.org/10.1029/2004sw000089
Witasse, O., Lilensten, J., Lathuillere, C., & Blelly, P.-L. (1999). Modeling the oi 630.0 and 557.7 nm thermospheric dayglow during eiscat-windii coordinated measurements. *Journal of Geophysical Research*, *104*(A11), 24639–24655. https://doi.org/10.1029/1999ja900260
Yerg, D. G. (1952). A tentative evaluation of kinematic viscosity for ionospheric regions. *Journal of Geophysical Research*, *57*(2), 217–220. https://doi.org/10.1029/jz057i002p00217
Zhang, K., Liu, J., Wang, W., & Wang, H. (2019). The effects of imf bz periodic oscillations on thermospheric meridional winds. *Journal of Geophysical Research: Space Physics*, *124*(7), 5800–5815. https://doi.org/10.1029/2019ja026527